UNIVERSITY OF CALABRIA

Physics Department

Philosophiæ Doctor Thesis in Physics XXII° Cycle

FIS/03

Implementation of CL apparatus coupled with a S.E.M.: results and applications

Doctoral School Coordinator
Prof. Giovanni Falcone

Candidate
Dr. Valentino Pingitore

Supervisor
Prof. Antonino Oliva

Contents

Introduction

The main scope of this work is to transform an old Scanning Electron Microscope (SEM) in an apparatus where it is possible also to perform Cathodo-luminescence (CL) measurements in addition to the usual investigations supplied by a standard SEM (SE-BSE, images, EDX analysis). The desired transformation has been conducted in a way that the resulting cost is rather low (order of thousands euro) in comparison to a standard SEM-CL apparatus, the cost of which is much higher (order of hundred thousands euro).

The work has been developed in three sections. In the first section the project was designed into details on the basis of the needed modification to be made on the SEM apparatus, verifying the possibility to allocate inside the main vacuum chamber a lens and an optical fiber and to have a feed through flange for transporting, via the optical fiber, the luminescence signal outside the chamber. To this purpose all the mechanical parts have been designed and fabricated in the department workshop using the appropriate vacuum compatible materials. Beside we proceeded in selecting and the purchasing the suitable spectrometer and the remaining equipment for data acquisition. Finally we selected the VS140 UV-VIS spectrometer by Horiba Jobin Yvon. Then all the system was assembled in its various components, allocated in the chamber and verified in functionality. In particular, many preliminary measurements have been carried out to focalize the optical components and to maximize the collected CL signal.

The second part of the work has been dedicated to obtain a standard protocol to acquire luminescence signals from "well known" luminescent materials and going to compare our measurements with referenced values used as standards, where "well known" in our case means the choice of materials for which the luminescent properties have been

extensively studied and available in literature.

The last section of the work is properly the research section where the acquired protocols have been applied to take measurements in different research fields, such as Solid State Physics, Earth Sciences and Cultural Heritage. Moreover, measurements of Mn^{2+} luminescence emission in calcite have been used to perform a calibration of our instrument by means of data acquired on the same materials using Laser-Induced Coupled Plasma analysis (LA-ICP), which is a technique very sensible to detect small traces of elements (up to $10 - 100$ *ppb*).

In chapter 1 we provide the theoretical background of the physical phenomenon of luminescence, starting from basic equations and going deeper inside the theory in order to achieve correct interpretations and assignment of spectra, especially in cases where no indications exist in literature.

Chapter 2 is dedicated to describe and illustrate all the transformations brought to the standard SEM apparatus to upgrade it for CL measurements. The description follows the steps implemented to modify the original SEM and the details of the optical configuration realized to obtain luminescence spectra generated by the energetic electron beam of the microscope, which can reach 40 keV.

In the last chapter we report our measurements carried out on various samples prepared and analyzed by the CL protocol as established in the first part of this work. The first results are dedicated to materials used to check the performances of the new system, comparing our acquired data with referenced values used as standards. Then we report the data relative to new investigations, in particular on materials for which luminescence data are scarce or even absent. Moreover we use the data on Mn to perform a calibration of our instrument and finally we report also an application to Cultural Heritage employing the CL technique to the analysis of an old coin.

Chapter 1

Theoretical aspects

From general considerations, the Hamiltonian of a free ion many-electron system can be written as

$$H_{fi} = H_0 + H_{er} + H_{so} \tag{1.1}$$

where H_0 is the kinetic and potential energy in the central field approximation, H_{er} is the residual Coulomb repulsion between the electrons and H_{so} is induced by spin-orbit coupling.

1.1 Central field approximation

In order to obtain a separable Schrödinger equation for a N electron system, an average (effective) spherical potential is assumed for each electron i *(central field approximation)*, generated by the nucleus charge and the other $N-1$ electrons *(self-consistent field approximation)*.

The Hamiltonian for a multi-electron system, neglecting spin and other relativistic effects is

$$H = \sum_i \left(-\frac{\hbar^2}{2\mu}\Delta_{ri} - \frac{Ze^2}{4\pi\varepsilon_0 r_i} \right) + \sum_{i<j} \frac{e^2}{4\pi\varepsilon_0 r_{ij}} \tag{1.2}$$

where μ is the reduced mass of the electron-nucleus system, r_i is the distance of the electron i to the nucleus of charge Ze and $r_{ij} = |r_i - r_j|$ is the distance between electron

i and j. The first term accounts for the *kinetic energy*, the second for the *nuclear potential energy* and the third for the *electron repulsion*.

The central field approximation assumes that the latter term contains a large spherically symmetric component, hence it can be written $H = H_0 + H_{er}$ with

$$H_0 = \sum_i \left(-\frac{\hbar^2}{2\mu}\Delta_{ri} - \frac{Ze^2}{4\pi\varepsilon_0 r_i} + U(r_i) \right) \tag{1.3}$$

$$H_{er} = \sum_{i<j} \frac{e^2}{4\pi\varepsilon_0 r_{ij}} - \sum_i U(r_i) \tag{1.4}$$

H_0 is a sum of terms for each electron, and the respective solutions of the time-independent Schrödinger equation can be written as product of the eigenstates of the single electron wave function

$$\psi_0 = \prod_i |n_i l_i m_l m_s\rangle \tag{1.5}$$

characterized by the principal quantum number n, the orbital angular momentum l_i, the magnetic quantum number m_l, and the spin quantum number m_s. The sub-index i is omitted for m_{l_i} and m_{s_i}. In the central field approximation, m_l and m_s are degenerate.

H_{er} is treated as a perturbation. $U(r)$ depends on the wave function of all electrons and can be solved iteratively by self-consistent field approach.

For more general system, the Hartree-Fock approach can be used to iteratively compute the potential in terms of perturbation theory, which takes into account exchange interaction.

Quantum numbers

The *quantum numbers* for H_0 in the central field approximation take values as follows:

- the principal quantum number $n = 1, 2, \ldots$
- the angular momentum quantum number $l = 0, 1, 2, \ldots, (n-1)$
- the magnetic quantum number $m_l = -l, (-l+1), \ldots, (l-1), l$
- the spin quantum number $m_s = \pm\frac{1}{2}$

The solution for central field approximation is degenerate in m_l and m_s.

1.2 Coupling schemes

The angular momenta of electrons in a partially filled sub-shell couple to total angular momenta, depending on the dominant interaction. The orbital motion and the magnetic spin moment are coupled via the magnetic interaction of the spin magnetic moment with the magnetic field of the orbital motion. Hence, consider the Hamiltonian $H = H_0 + H_{er} + H_{so}$ with

$$H_{so} = \sum_{i=1}^{N} \xi\left(r_i\right)\left(\vec{l_i} \cdot \vec{s_i}\right) \tag{1.6}$$

ξ is the spin-orbit coupling constant of the particular system

$$\xi\left(r\right) = \frac{\hbar^2}{2m^2c^3r}\frac{d}{dr}U(r)$$

$\vec{l_i}$ the orbital momentum and $\vec{s_i}$ the spin of electron i.

LS coupling

For ions with small Z the most important residual interaction is the electrostatic repulsion between electrons.

$$H_{er} \gg H_{so}$$

in this case the eigenstates of $H_0 + H_{er}$ are considered, treating H_{so} as a perturbation. The ordering of the energy levels is given by *Hund's rule*. The orbital angular momenta are coupled first to form the total orbital angular momentum $\vec{L} = \sum_{i=1}^{N} \vec{l_i}$. The spin angular momenta are summed likewise to the total spin angular momentum $\vec{S} = \sum_{i=1}^{N} \vec{s_i}$. The total spin orbital momenta finally couple to $\vec{J} = \vec{L} + \vec{S}$.

This is known as the *Russel-Saunders approximation* or LS coupling. The resulting states are described by their basis function ${}^{2S+1}L_J$, which is $(2J+1)$-fold degenerate in M_J.

jj coupling

In ions with large Z values the spin-orbit coupling is much stronger than residual Coulomb interaction:

$$H_{er} \ll H_{so}$$

It is appropriate to couple the spin and orbital angular momenta of each electron separately $\vec{j_i} = \vec{l_i} + \vec{s_i}$, yielding the total angular momentum $\vec{J} = \sum_{i=1}^{N} \vec{j_i}$. The basis function is denoted by $[(l_1, s_1)\, j_1, \ldots, (l_N, s_N)\, j_N]\, J$. The jj coupling case is usually only considered for heaviest elements, i.e. the actinides, or for lighter atoms in highly ionized states.

Intermediate coupling

The $4f$ rare earth ions are a case of intermediate coupling, neither LS nor jj coupling are appropriate. The eigenfunctions can be expressed in a different basis set, commonly denoted in terms of Russell-Saunders states $^{2S+1}L_J$. The theoretical treatment is more advanced, however, and beyond the scope of this thesis.

1.3 Ions in a static crystal field

Optically active ions incorporated in a crystal lattice experience interactions with lattice, which influences the optical properties described by

$$H = H_{fi} + H_{cf} \tag{1.7}$$

where $H_{fi} = H_0 + H_{er} + H_{so}$ is the free-ion Hamiltonian (Equation 1.1) and H_{cf} accounts for the static crystal field interaction.

The changes introduced into the energy level structure depend on the magnitude of each quantity. Two cases will be discussed:

- the strong ligand field ($H_{so} \ll H_{cf}$), which has to be considered for $3d$ transition metals

- and the weak ligand field ($H_{so} \gg H_{cf}$), which is appropriate for the rare earths.

The inter-configurational $4f \rightarrow 5d$ transitions of the rare earths are also strongly influenced by the crystal field.

1.3.1 Transition metal ions in a static crystal field

The spin-orbit coupling in $3d^n$ transition metals ($\approx 100\ cm^{-1}$) is much weaker than the large contributions of the crystal field ($\approx 10^4\ cm^{-1}$) and therefore neglected,

$$H_{so} \ll H_{cf} \tag{1.8}$$

Thus, the splitting energy and degeneracy are determined by the crystal field strength and symmetry. It should be noted that spin-orbit coupling has to be considered again for discussing splitting of sharp lines and transition probabilities between the energy levels.

The weak, medium, and strong field cases of crystal field and electrostatic repulsion interaction of the electrons are distinguished.

Medium crystal field

If the crystal field energy is of the same order as the residual electron repulsion,

$$H_{cf} \approx H_{er}$$

the configuration interaction between states of the same reduced representation but of different electronic configuration needs to be considered.

Weak crystal field

If the crystal field energy is much smaller than the residual electrostatic interaction,

$$H_{cf} \ll H_{er}$$

the levels can be denoted according to their free ion terms (^{2S+1}L) which are $(2S+1)(2L+1)$ degenerate.

Strong crystal field

If the crystal field energy is much larger than the residual electrostatic interaction between the electrons,

$$H_{cf} \gg H_{er}$$

the energy levels are only determined by the number of electrons in t_2 and e orbitals and split in $(2S+1)(\Gamma)$ degenerate $^{2S+1}\Gamma(t_2^n e^{N-n})$.

	O_h	T_d	D_{4h}
S	A_{1g}	A_1	A_{1g}
P	T_{1g}	T_{1g}	$A_{2g} + E_g$
D	$E_g + T_{2g}$	$E + T_2$	$A_{1g} + B_{1g} + B_{2g} + E_g$
F	$A_{2g} + T_{1g} + T_{2g}$	$A_2 + T_1 + T_2$	$A_{2g} + B_{1g} + B_{2g} + 2E_g$
G	$A_{1g} + E_g + T_{1g} + T_{2g}$	$A_1 + E_g + T_1 + T_2$	$2A_{1g} + A_{2g} + B_{1g} + B_{2g} + 2E_g$
H	$E_g + 2T_{1g} + T_{2g}$	$E + T_1 + 2T_2$	$A_{1g} + 2A_{2g} + B_{1g} + B_{2g} + 3E_g$

Table 1.1: Splitting of $3d$ terms in O_h, T_d and D_{4h} symmetry. States of odd parity have been omitted. The spin multiplicity (omitted) of free ion states is conserved for crystal field terms.

By crystal field perturbation these levels split in sub-levels denoted by $(^{2S+1}\Gamma)(^{2S+1}L)$, which is shown in Table 1.1 for terms in d configuration in local symmetries O_h (octahedral), T_d (tetrahedral) and at lower symmetry D_{4h}. The spin multiplicity of free ion states is conserved for crystal field terms. For example in O_h symmetry S and P states do not split (yielding A_{1g} and T_{1g} levels, respectively), while D states result in two terms E_g and T_{2g}. $(^{2S+1}\Gamma)$ represent terms adopted from the Mulliken symbols for atomic and molecular orbitals:

A	non-degenerate orbital, symmetric to the principal axis C_n
B	non-degenerate orbital, anti-symmetric to the principal axis C_n
E	doubly degenerate orbital
T	triply degenerate orbital
g	(subscript) symmetric to center inversion (*gerade parity*)
u	(subscript) anti-symmetric to center inversion (*ungerade parity*)
1	(subscript) symmetric with respect to axis C_2 perpendicular to C_n
2	(subscript) anti-symmetric with respect to axis C_2 perpendicular to C_n

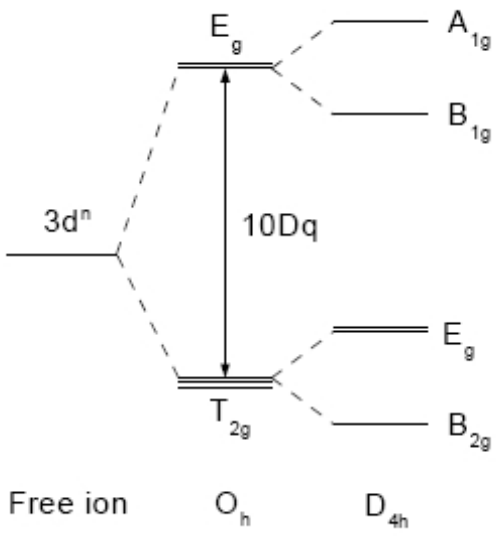

Figure 1-1: Splitting of the $3d^n$ free ion level by crystal field in O_h and D_{4h} symmetry

A $3d^n$ free ion level is split by the crystal field in O_h (octahedral) local symmetry in the E_g and T_{2g} sub-levels which are doubly and triply degenerate, respectively (Figure 1-1). if the symmetry is lowered to D_{4h} (square planar) the terms found in octahedral configuration are further split into two sub-level each.

In the weak, intermediate and strong crystal field radial and angular part of the electron repulsion interaction can be represented as a linear combination by the Slater-Condon-Shortley parameters F_0, F_2 and F_4. Racah recognized that the relationships $B = F_2 - 5F_4$ and $C = 35F_4$ appeared frequently. Thus, a substitutional set of *Racah parameters B, C* and *crystal field splitting parameter Dq* is used for spectroscopic purposed,

where energy differences are measured.

Tanabe and Sugano calculated the determinants of the interactions for d^2 to d^8 configuration in octahedral symmetry [1]. The results are depicted in Tanabe-Sugano diagrams [2], which have been employed for quantitative evaluation of the spectra.

Ground state splitting

In the free ion all five d orbitals are degenerate. The non-spherical environment in local surrounding introduces a ground state splitting in ions with more than one d electron into two sub-set, a triply degenerate t_{2g} and doubly degenerate set labeled e_g [3]. The energy separation designated by $10Dq$ is typically of the order of several thousand wavenumbers in fluorides [4].

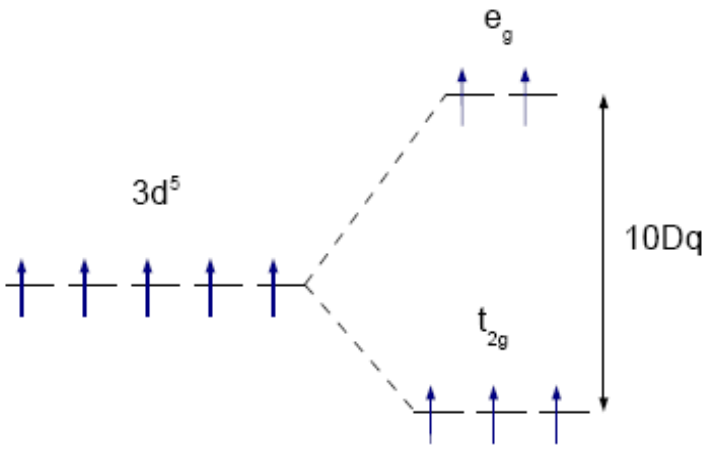

Figure 1-2: Ground state splitting of d^5 ions in crystalline environment into the lower triply degenerate t_{2g} and the upper doubly degenerate e_g level.

In a weak crystal field usually met in fluorides Mn^{2+} manifest in the high-spin ground state, which is split into the lower triply degenerate t_{2g} and the higher doubly degenerate e_g sub-level as showed in Figure 1-2.

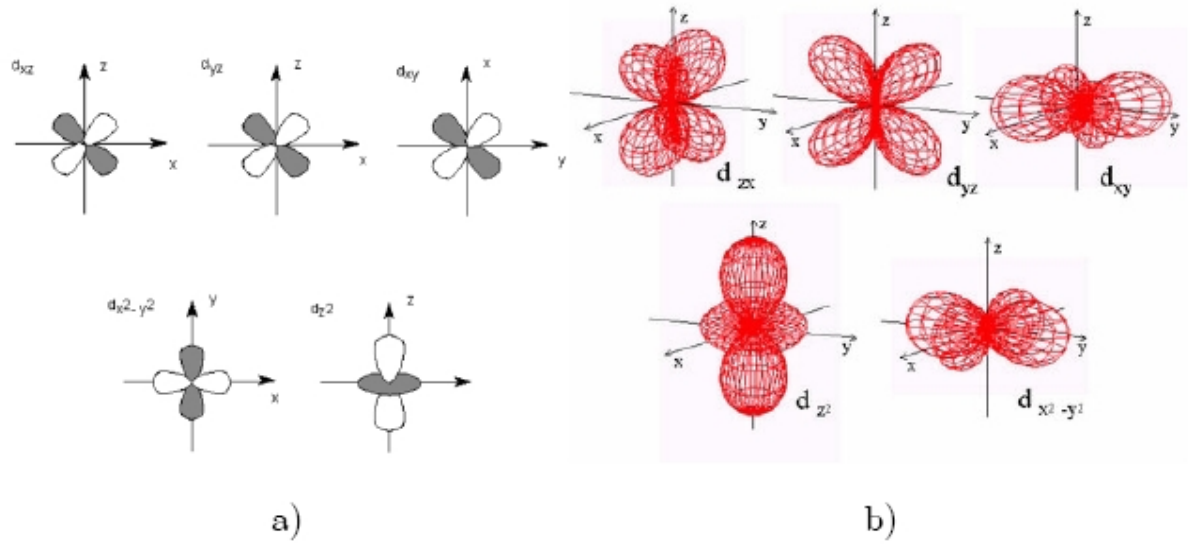

Figure 1-3: 3*d* orbital 2D view a) and 3D view b)

The crystal field splitting in a tetrahedral symmetry is intrinsically smaller than in the octahedral symmetry as there only four ligands (instead of six ligands in the octahedral symmetry) interacting with the transition metal ion.

When a transition cation belongs to an octaedrical coordination environment with 6 identical ligands localized along the cartesian axis in the octaedrical vertices the e^- of the 3*d* orbitals suffer a repulsion from the anions or from the dipolar ligands and the orbital energetic level is lowered (Figure 1-3). Since the orbital lobes are towards the ligands, the orbital electrons suffer a repulsion which is greater than the others 3*d* orbitals. Then the energy of the e_g orbitals is greater than that of the t_{2g} orbitals. The e^- in the t_2 orbitals (such nomenclature is due to the lack of a symmetry center) are subject to a more intense repulsion as compared to the orbital electrons and this fact determines an inversion in the energetic levels with respect to the octahedral symmetry. In polyedral systems with a symmetry center, the ligands being in the vertices, the energies of the e_g and t_{2g} orbitals are allocated as in the tetrahedral symmetry (Figure 1-4), even if with different values of the separation parameters $10Dq \equiv \Delta$:

$$\Delta_{oct} : \Delta_{cub} : \Delta_{tetr} = 1 : \frac{8}{9} : \frac{4}{9} \tag{1.9}$$

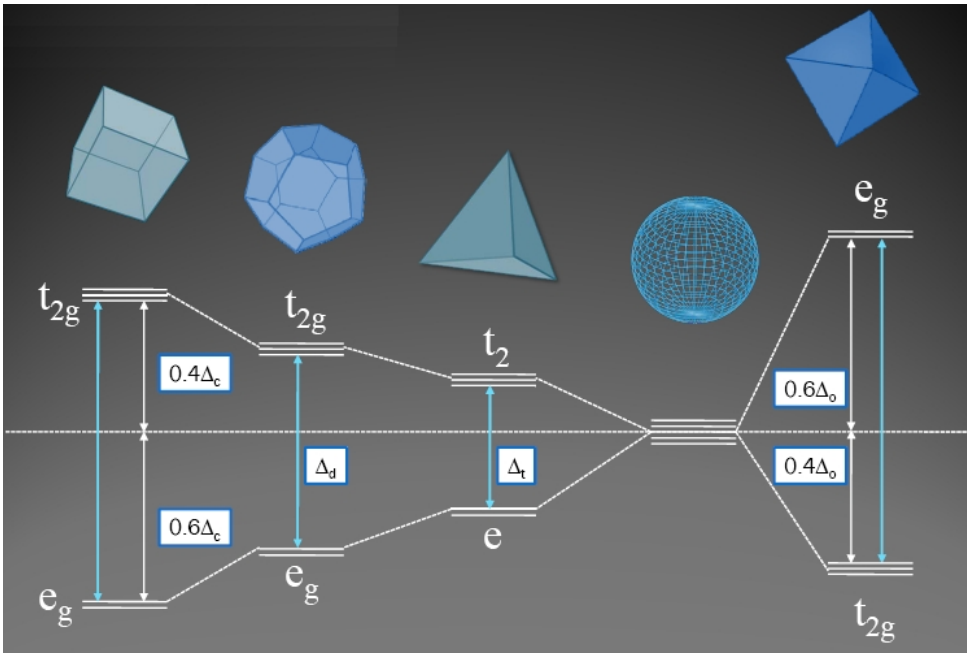

Figure 1-4: Splitting of the five d-orbital in various types of ligand fields [5]

Reading Tanabe-Sugano Diagrams

Tanabe and Sugano taking the mutual interactions between the d-electrons as well as the crystal field into account have calculated the energy levels originating from such a configuration (in Figure 1-5 is shown d^4 diagram). On the utmost left-hand side where the crystal field $\Delta = 0$ we find the energy levels of free ion. Many of these levels split into two or more levels for $\Delta \neq 0$.

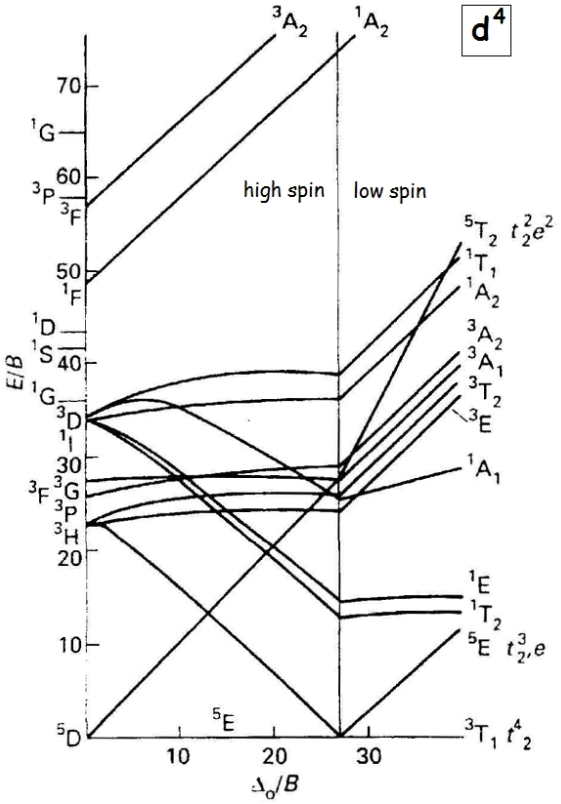

Figure 1-5: Tanabe-Sugano diagrams for d^4 transition elements [6]

The lowest level, i. e. the ground state, coincides with the x-axis. For the free ion the levels are marked ^{2S+1}L, where S presents the total spin quantum number, and L the total orbital angular momentum. Values of L may be $0(S)$, $1(P)$, $2(D)$, $3(F)$, $4(G)$, etc. The degeneracy of these levels is $2L + 1$ and maybe lifted by the crystal field. Crystal field levels are marked X^{2S+1}, where X may be A (no degeneracy), E (two fold degeneracy) and T (tree fold degeneracy). Subscripts indicate certain symmetry properties. g indicates symmetric to center inversion (*gerade parity*), u anti-symmetric to center inversion (*ungerade parity*), 1 symmetric with respect to axis C_2 perpendicular to C_n and 2 anti-symmetric with respect to axis C_2 perpendicular to C. Usually, in Tanabe-Sugano diagrams the energy is plotted against the crystal field splitting $10Dq$, both in units of the Racah parameter B. B represent interelectron repulsion parameter and then $B_{\text{complex}} < B_{\text{free ion}}$. For a given transition metal ion the bond covalency depends on the ligand ions, which are arranged in the order of B decreasing in so-called nephelauxetic

series:

$$\xrightarrow[\qquad\qquad\qquad\qquad\qquad\qquad\qquad\qquad\qquad\qquad\qquad\qquad\qquad\qquad\qquad\qquad\qquad\qquad]{B_{\text{complex}}}$$

$$Se^{2-} \quad I^- \quad Br^- \quad Cl^- \quad O^{2-} \quad F^-$$

$$\xleftarrow[\qquad\qquad\qquad\qquad\qquad\qquad\qquad\qquad\qquad\qquad\qquad\qquad\qquad\qquad\qquad\qquad\qquad\qquad]{\text{covalency}}$$

The values of the crystal field splitting $10Dq$ within equivalent surroundings are of the order

$$Mn^{2+} < Ni^{2+} < Co^{2+} < Fe^{2+} < V^{2+} < Fe^{3+} < Cr^{3+} < V^{3+} < Co^{3+} < Mn^{4+} \quad (1.10)$$

in fact $10Dq$ is determined by the effective charge of the ligands Q, by the average radius of the d-orbital and by the ligand-metal distance R:

$$10Dq \approx Q\frac{\langle r^4 \rangle}{R^5}$$

Degenerate orbitals are filled according to *Hunde rules*: one electron is added to each of the degenerate orbitals in a subshell before a second electron is added to any orbital in the subshell; electrons are added to a subshell with the same value of the spin quantum number until each orbital in the subshell has at least one electron. But such a filling scheme is valid only for the high spin (or low field) configurations. If there is a large enough energy difference between the five d orbitals, as in the case if the ligand field is very large, Hund's rule of maximum multeplicity no longer applies. As a result, the lower orbitals, for example the three t_{2g} orbitals in a octahedral system, will fill completely before any electrons enter the upper two e_g orbitals. This is a low spin (or high field) configuration. Significant changes could occur in the octahedral $3d^4$ to $3d^7$ cases, and in tetrahedral $3d^3$ to $3d^6$ cases.

Because energy octahedral separation is opposite respect tetrahedral cubic cases (Figure 2.4) $3d^n$ Tanabe-Sugano diagrams (indicated with TS^n) follow this rule

$$TS^n_{oct} = TS^{10-n}_{tetr} = TS^{10-n}_{cub}$$

with,obviously, different separation energies for each symmetry.

1.4 Ions in a vibrating lattice

If an ion as optically active center is incorporated in a crystal, the lattice vibrations (phonons) influence the spectra. The additional term supplementary to the static crystal field Hamiltonian yields

$$H = H_{fi} + H_{cf} + H_{ep} \tag{1.11}$$

H_{fi} is the free ion Hamiltonian (Equation 1.1), H_{cf} accounts for the static crystal field (Equation 1.7) and H_{ep} is the kinetic and "interionic" energy of the lattice ions. It is should be noted that the free ion crystal field Hamiltonian depends both on the electronic and ionic coordinates.

Lattice vibrations can be depicted as periodic displacement of ions. The interaction between the electronic state and the vibrating modes of crystal lattice (phonons) is determined by the *electron-phonon coupling*. Certain simplifications lead to the *configuration coordinate model* [7].

The simplest case is a linear chain of identical atoms at equilibrium distance a with nearest-neighbor harmonic interaction. The corresponding Hamiltonian describes a coupled mode of oscillation with a normal coordinate Q_{k_n}. The solution of the corresponding Hamiltonian are *phonons*, quanta $|n_k\rangle$ of vibrational energy $\sum \left(n_k + \frac{1}{2}\right) \hbar\omega_k$, representing the eigenstates as product $\prod |n_k\rangle$.

Electron-phonon coupling

The interaction of an optically active ion with the dynamic lattice is described by

$$H_{ep} = \sum_k \left(\frac{p_k^2}{2M_k} + V_{pot}(r_{k,0} + q_k) \right) \tag{1.12}$$

where p_k is the momentum of the r^{th} oscillating ion with mass M_k, $r_{k,0}$ is its equilibrium position, and q_k is the displacement.

In order to solve the corresponding Schrödinger equation, the *Born-Oppenheimer* or *adiabatic approximation* [8] is introduced to decouple the electronic and ionic coordinates.

Under the resonable assumption that ionic motion is much slower than electron motion, the eigenstates can be expressed as product terms of the electronic and vibrational functions (*Born-Oppenheimer states*). Usually one representative vibrational lattice mode is chosen, the *breathing mode* A_{1g} (Figure 1-6), in wich the ligands pulsate symmetrically about the optically active ion. The distance of this ion to the first ligand is defined as configurational coordinate Q.

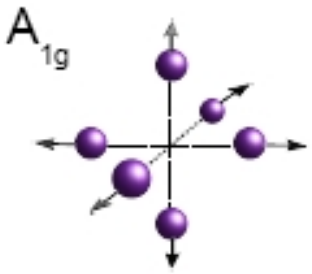

Figure 1-6: A_{1g} vibrating mode of an optically active ion surrounded by six ligands

Configuration coordinate diagram

Figure 1-7 shows two electronic states in the *single configuration coordinate diagram* (with equilibrium positions of the ground state $Q = 0$ and excited state Q_0, respectively, where the configuration coordinate Q represents the *deviation* of ion-ligand distance from its equilibrium position. A large difference ΔQ of two states corresponds to a strong electron-phonon coupling. The transition of an electron from the lower to the upper configuration at $Q = 0$ is indicated by an arrow. A higher vibrational mode of the upper configuration is excited predominantly, which will subsequently relax to the lowest vibrational state.

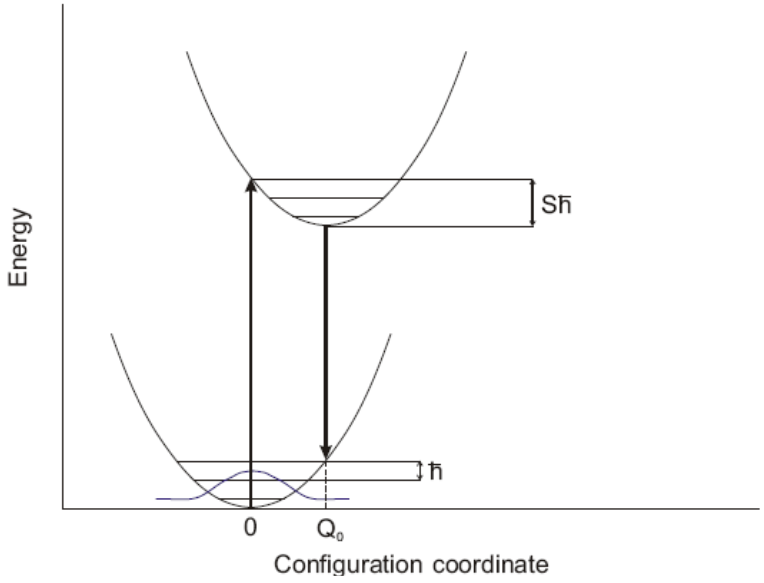

Figure 1-7: Single configuration coordinate diagram of two electronic states at equilibrium positions $Q = 0$ and $Q = Q_0$. S denotes the $Huang - Rhys$ factor.

Subsequent emission to the ground state occurs at lower energy than in excitation, which is known as Stokes' shift [7].

This model is often used to discuss optical properties, and several observations can be explained:

- Stokes law,
- the widths of absorption or emission bands and their temperature dependence,
- quenching of luminescence induced by temperature.

The strength of electron-lattice coupling is described by the *Huang-Rhys* factor

$$S = \frac{1}{2}\frac{M\omega^2}{\hbar\omega}\left(Q - Q_0\right)^2 \tag{1.13}$$

where M is the effective ionic mass, ω is the vibrational frequency, and Q_0 is the coordinate of the equilibrium position of the excited state. The vertical line at $Q = 0$ intersects the upper parabola at the higher vibratinal level $S\hbar\omega$.

The *Huang-Rhys* factor S is correlated to the number of emitted phonons as can be

seen in Figure 1-8. The upper part ($S = 20$) shows a rich phonon structure, while little intensity is contained in the ZPL. In compounds having weak phonon-interaction the ZPL becomes much more pronounced ($S = 2$).

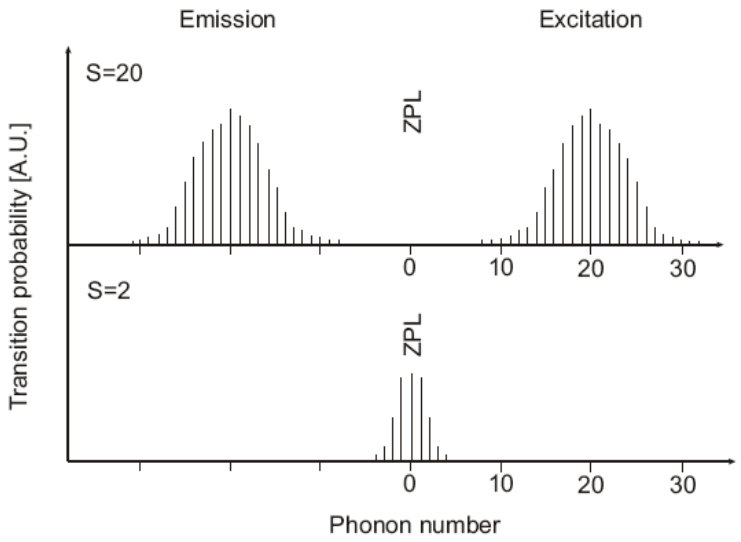

Figure 1-8: Calculated spectral shape in the configuration coordinate model for $S = 20$ (upper graph) and $S = 2$ (lower graph). Values taken from [9]

The emission (on the left) as well as excitation (right) transition probabilities in the configuration coordinate model are shown, neglecting selection rules and line widths of transitions. The ZPL results from the radiative transition between the lowest vibrational modes of different electronic states, i.e. without involving phonons [10]. Thus, the energy of the ZPL is equal in excitation and emission. Its intensity equals $I_0 = e^{-S}$, I_0 being the total intensity. If the ground state of two electronic states coincide $Q = Q_0$, the Huang-Rhys parameter becomes $S = 0$ and all intensity I_0 is contained in the ZPL.

For $S > 0$ the intensity of the ZPL is reduced and phonon sidebands appear on the low-energy side in emission. At elevated temperature additional anti-Stokes sidebands are observed on the opposing side of the ZPL. In the strong coupling case in emission and excitation spectra only structureless bands show up that cannot be resolved due to strong phonon sidebands.

Considering real crystals, not only the breathing mode, but also many vibrational modes are present. Therefore, besides temperature effects, the vibronic sidebands will appear broader. The ZPL ($m = 0$) has the natural (experimental) line width, vibronics ($m \lesseqgtr 0$) have larger widths $m\hbar\omega$ due to coupling to the lattice, according to [7]. In practice, the description given by the single configuration coordinate diagram is not suitable for describing phonon energies, since coupling to one breathing mode is not representative for the whole spectrum and selection rules may change the observation considerably.

1.5 Radiative transitions

Selection rules

Electronic transitions observed are primarily of electric or magnetic dipole character, merely quadrupole transitions may play a subordinate role. Regarding the corresponding oscillator strengths, magnetic dipole transitions are of the order of 10^{-8}, electric dipole transition rather 10^{-5} to 10^{-8} [7]. Judd and Ofelt found theoretically an expression for the oscillator strength between electric dipole transitions of the ground configuration $4f^N$, assuming small extension of excited configurations [11][12]. In the Russell-Saunders approximation, the following selection rules apply.

Laporte (symmetry) selection rule

The orbital quantum number l for electric dipole transitions has to change according to

$$\Delta l = \pm 1$$

In other words, the initial and final states must have opposite parity. Due to several interactions with the electronic wave function of the ion, however, the Laporte selection rule is relaxed [13]:

1. *Electron-phonon interaction.* In the case of an octahedral surrounding, e.g., there

exist gerade (even) and ungerade (odd) type vibrational modes. Hence, even type transitions gain partly odd character and become allowed by coupling to vibrational modes.

2. *Interaction with higher orbitals.* By mixing with the wave function of higher orbitals, e.g. d and p orbitals, odd character can be added to the wave function. This interaction is depending on the symmetry and is, in general, more pronounced in non-centrosymmetric surroundings.

3. *Interaction with ligand orbitals.* Contrary to purely ionic crystals, covalency accounts for mixing with the wave function of the ligands, thus possibly introducing odd character to the optically active ion.

In local surroundings without inversion symmetry the Laporte selection rule is further relaxed by admixture of states having opposite parity compared to the $4f^N$ states. Consequently, $f \rightarrow f$ transitions are observed much weaker on lattice sites having inversion symmetry.

Spin selection rule

Electric dipole transition require the spin to be conserved.

$$\Delta S = 0$$

The spin-selection rule is relaxed in presence of spin-orbit coupling, since the wave function cannot be factorized strictly to $\psi = \psi_{space} \cdot \psi_{spin}$. Hence, spin-forbidden features are expected in the spectra. For transition metal with weak spin-orbit coupling they appear as weak bands, whereas intensity for rare earths is somewhat increased due to the stronger spin-orbit coupling.

Selection rule for the total quantum number J

In the case of $4f$ rare earth the selection rule derived by Judd and ofelt [11][12] from calculations of crystal spectra intensities become for *electric dipole transitions*

$$\Delta J \leq 6$$

with the excepction of the following $J \rightarrow J$ transitions: $0 \rightarrow 0$ is forbidden, and $0 \rightarrow 1$, $0 \rightarrow 3$, $0 \rightarrow 5$ appear extraordinary weakly in RE ions having an even number of electrons [14].

For magnetic dipole transitions the selection rule reads

$$\Delta J = 0, \pm 1$$

with the exception of the $J \rightarrow J$ transitions $0 \rightarrow 0$.

1.6 $^4T_{1g}(G) \rightarrow ^6 A_{1g}(S)$ transition for Mn^{2+}

In Figure 1-9 is shown Tanabe -Sugano diagram for d^5 elements.

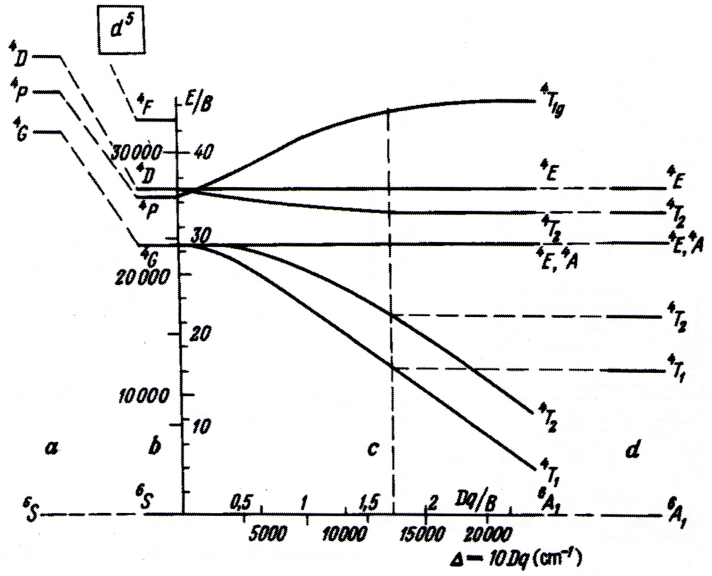

Figure 1-9: Tanabe -Sugano diagram for d^5 elements

The electronic transition $^4T_{1g}(G) \rightarrow^6 A_{1g}(S)$ (responsible for luminescence in Mn^{2+} centres) is spin-forbidden and also Laporte forbidden for electric dipole transitions on account of the centre of symmetry. Magnetic dipole transition, which is Laporte allowed in a centrosymmetric site, has a much lower probability than an electric dipole transition.

In comparison with $4f$ elements, the $3d$ transition metals show a much stronger electron-phonon coupling. Hence the rich energy level structure of Mn^{2+} allows nonradiative relaxation even at liquid helium temperature to the lowest excited state $^4T_{1g}(G)$ and subsequent emission $^4T_{1g}(G) \rightarrow^6 A_{1g}(S)$ to the ground state. Several emission bands at different energies are observed, if Mn^{2+} is incorporated into different crystallographic sites. The emission bands have typically a FWHM of 1000 to 2000 cm^{-1} without any features, and are of a non-Gaussian Pekarian shape [7]. This is due to the strong electron-phonon coupling of the $3d$ ions which prevents the observation of sharp electronic or vibrational lines, as opposed to rare earth ions.

In various crystals zero-phonon transitions have been observed at low temperature and rather low concentrations. Detailed vibronic fine structure was observed and first assigned to phonon-coupled electronic transitions in Mn^{2+} doped ZnS [15]. Hence, the non-Gaussian shape of the broad band emission was attributed to the vibronic structure. At low temperature a steep raise on the high-energy side is caused by the zero-phonon transition. At higher temperature the band is extended towards the high-energy side as anti-Stokes' emission is activated, approaching the Gaussian shape to some degree.

The spin-forbiddingness is broken down to some extent by a small degree of spin-orbit coupling, but the long decay times of Mn^{2+} luminescence and the weakness of the corresponding absorption transitions are a consequence of such forbiddingness [16].

Changes in coordination, such as from octahedral to tetrahedral, produce a considerable change in D_q. The tetrahedral D_q value is smaller and the energy of all of the transitions in Mn^{2+} increase.

The calcite group of minerals (which includes magnesite and rhodochrosite) has a rhombohedral structure and the unit cell contains two molecules. The essentially planar and triangular carbonate groups lie perpendicular to the three-fold axis. Each calcium

(or other metal cation) is surrounded by six oxygen ligands in octahedral coordination; the octahedron is however, trigonally distorted, being slightly elongated along the above-mentioned triad axis, and lies between two carbonate planes. Although the site closely approximates to O_h symmetry, the actual point symmetry is D_{3d}. There are, therefore, six equal metal-oxygen distances (see Table 2.2) and the site remains strictly centrosymmetric.

The dolomite structure is slightly different in that magnesium and calcium atoms are ordered in alternate layers perpendicular to the principal axis, although in practice, the ordering and stoichiometry of Mg and Ca atoms is seldom perfect. Nevertheless, the Mg and Ca sites are quite different in size, the Mg site being slightly smaller than in magnesite and the Ca site slightly larger than in calcite (see Table 1.2). Both sites, however, once again remain centrosymmetric having S_6 point symmetry.

	cation-anion distance ($\mathring{A}$)	$10Dq$ (cm^{-1})	$\Delta 10Dq$ (cm^{-1})	B (cm^{-1})	ΔB (cm^{-1})
calcite	2.36	7100	200	850	20
magnesite	2.10	8500	200	840	20
dolomite (Mg-site)	2.09	8500	200	840	20
dolomite (Ca-site)	2.38	6600	200	850	20
rhodochrosite ($MnCO_3$)	2.19	8300	200	800	20

Table 1.2: Ligand-field parameters for Mn^{2+} in carbonates, obtained from excitation spectra [17]

For six-fold (octahedral O_h) coordination, the Ca^{2+} lattice site is considerably larger (ionic radius 114 pm) compared to Mn^{2+} (ionic radius 81 pm), which is favorable for substitution of this ion [18].

1.7 Luminescence in the Band Scheme

Atoms in minerals are very close and influence each other strongly. As a result in certain minerals the energy levels of individual atoms are combined and form energy zones filled by electrons. The inner atom orbitals of the individual atoms form inner energy zones totally filled by electrons. The outer atom orbitals from the outer energy zones filled by electrons (Figure 1-10). The last filled zone is called the valence band (VB) because valence electrons take part in its occupation. The higher energy zones, following the valence zone, are empty because they are formed by empty electron orbitals. The lowest of these zones is called the conduction band (CB). The energy interval between the valence zone and conductivity zones is called the forbidden zone and designated as E_g.

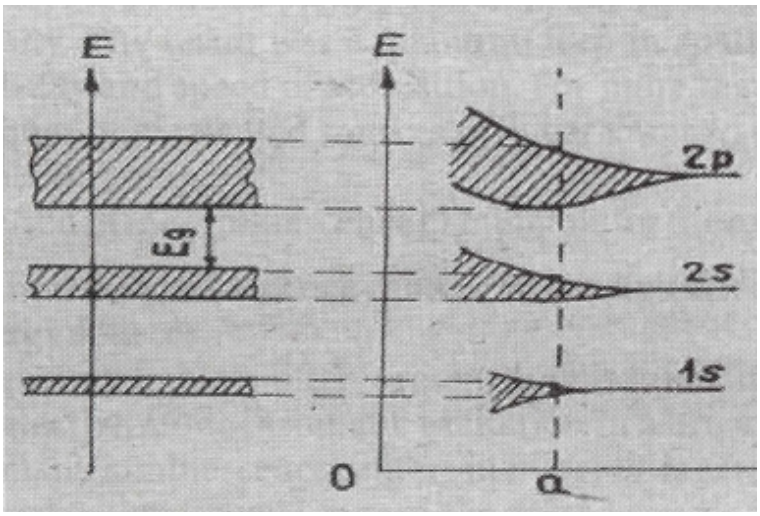

Figure 1-10: Energy zones formation scheme

With small dimensions of the forbidden band the electron transfer of the impurity or the main substance to the conduction band may take place. The most important luminescent minerals of this kind are ZnS and silver bromides. With interband spacing of $3-4$ eV a UV irradiation with a wavelength of less than 300 nm has enough energy to detach electrons and transfer them from the filled valence band into an empty conduction band. Thus we have a free electron in the conduction band and a free hole in the valence band. The certain defects may catch a free electron, forming an electron center,

or a free hole forming a hole center. Upon disappearance of such centers, as a result of recombination with the opposite charge carrier, recombination energy serves as the excitation source for the luminescence center and emission appears.

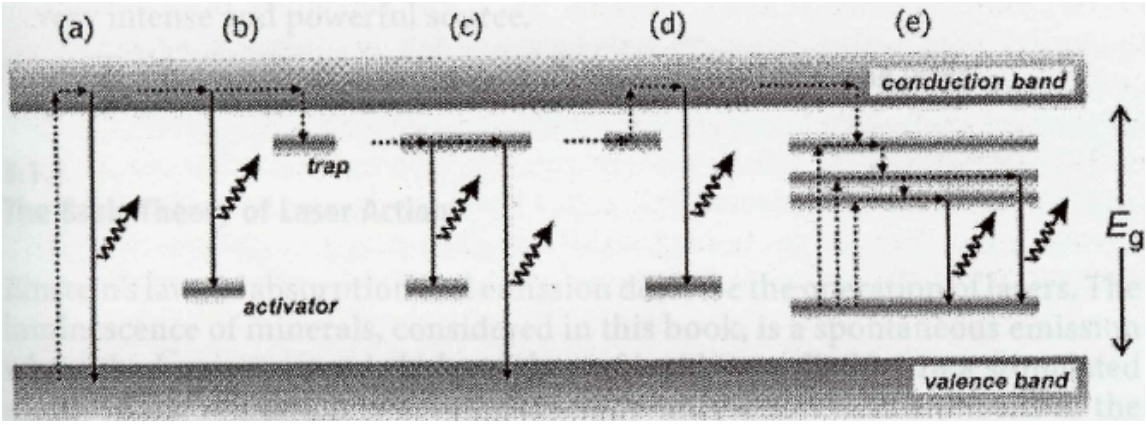

Figure 1-11: Simplified sketch of electron band structure of a semiconductor mineral, showing the process of excitation (energy absorption), non-radiative energy transfer and generation of luminescence

The following processes are possible:

- "Intrinsic" luminescence where an electron is excited from the valence band to the conduction band, so called *interband transition*. Recombination of this electron with a hole in the valence band generates a photon, the energy of which corresponds to the energy difference of the band gap (Figure 1-11 a);

- The excited electron may also recombine with an activator, with the following luminescence, or a trap, with the following electron capturing, within the forbidden gap. Traps and activator energy levels are caused by defects in the crystal lattice (Figure 1-11 b);

- Luminescence generation through direct recombination of electrons from a trap with an activator (tunneling) or with a hole in the valence band (Figure 1-11 c);

- Stimulated release from an electron from the trap to the collection band, followed by emissive recombination with an activator. This process is called thermoluminescence (electron release stimulated by heating) and optically stimulated luminescence (electron

release stimulated by light) (Figure 1-11 d);

- "Extrinsic" luminescence, where after being excited, electrons of defect ions recombine with the ground state with luminescence emission (Figure 1-11 e).

1.8 Rare earth ions in a static crystal field

The $4f^n$ shell is well shielded by filled outer $5s$ and $5p$ orbitals as shown for Gd^{3+} in Figure 1-12. For the trivalent RE the situation is very similar, except for the missing $5d$ shell.

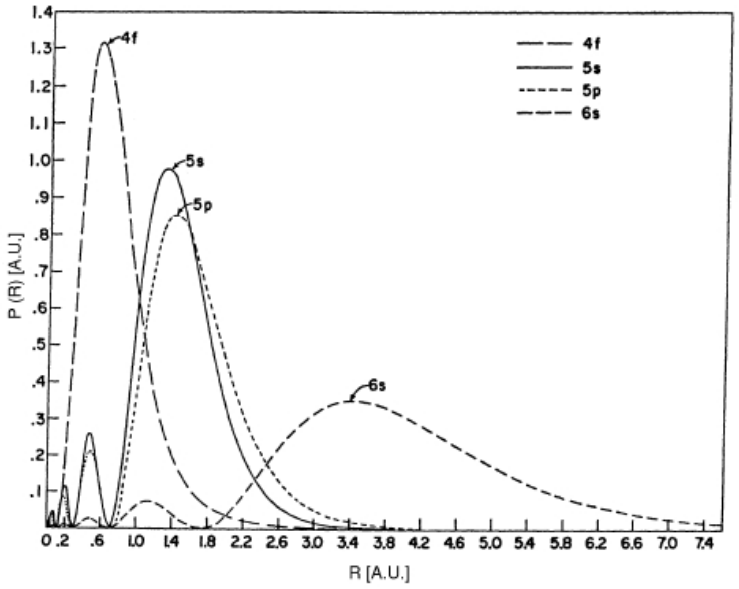

Figure 1-12: Radial charge distribution $P(R)$ of the Gd^{3+} radial wave function for $4f$, $5s$, $5p$, and $6s$ orbitals. R is the distance from the nucleus [14]

The $4f$ energy levels of free RE ions are only slightly perturbed by the crystal field, and the energies do not change much with changing the ligands. In high resolution measurements, however, considerable variations are observable. The shielding effect decreased with increasing atomic number [19].

Assuming Russell-Saunders coupling the crystal field splitting ($\approx 100\ cm^{-1}$) is much lower than spin-orbit coupling ($\approx 1000\ cm^{-1}$) or the term separation ($\approx 10000\ cm^{-1}$),

corresponding to the order (Figure 1-13)

$$H_{cf} \ll H_{so} \ll H_0$$

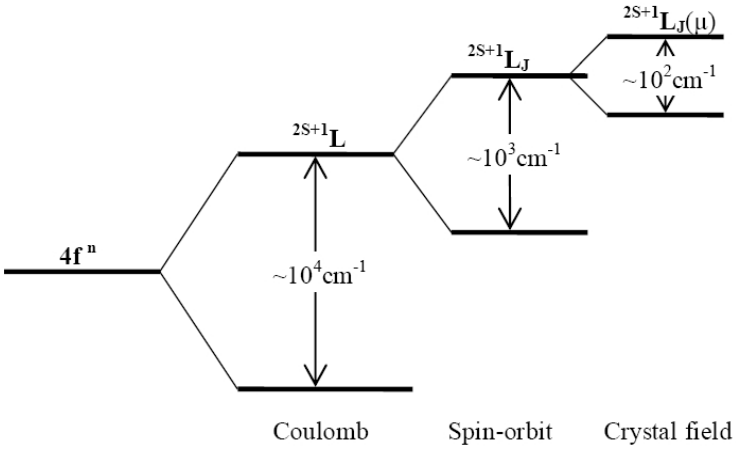

Figure 1-13: Energy splitting for REE

The outer $5d$ shell is much more sensitive to the crystal field, since it is not shielded by filled $5s$ and $5p$ orbitals. Therefore, the $4f \rightarrow 5d$ transition energies are shifted considerably by the crystal field of the surrounding. In order to determine the energy levels and eigenfunctions of RE ions in a lattice, the matrix elements of the perturbed Hamiltonian can be calculated in the one-electron approximation. The crystal field Hamiltonian can be written

$$H_{cf} = \sum_{k,q} B_q^k \hat{C}_q^k \tag{1.14}$$

where B_q^k are parameters containing the structure of the local crystal field, and $\hat{C}_q^k$ are tensor operators [20]. This accounts for the nephelauxetic effect, introducing a red-shift to the free ion levels and further lifting of the M_j degeneracy. The red-shift increases with increasing covalency of the surroundings. For the rare earth ions the $4f$ levels only experience a weak nephelauxetic effect due to the shielding of $5d$ orbitals.

Inter-configuration $4f^{n-1}5d \rightarrow 4f^n$ transitions

The $5d \rightarrow 4f$ transitions in RE ions are observed in vacuum ultraviolet (VUV) spectral region below 200 nm. The energy of these transitions depends more on the local environment then that $4f$ states, since they are not shielded by filled outer shells.

Cerium

In Ce^{3+} the $5d \rightarrow 4f$ transition energy is the lowest among the RE ions. The closest $4f$ level $^2F_{7/2}$ is still much lower in energy. The energy level of the valence electron $5d$ of Ce^{3+} in the excited state is split into two levels, T_{2g} and E_g, separated by the crystal field parameter $10Dq$, while the energy level of the valence electron $4f$ of Ce^{3+} in the ground state is split into two levels, $^2F_{7/2}$ and $^2F_{5/2}$. The emission transitions, therefore, are attributed to the transitions from the lower E_g level to $^2F_{7/2}$ and $^2F_{5/2}$ (the downward arrows in Figure 1-14). Although the content of Ce is usually low in natural calcite (from some ppb to some ppm), observation of the Ce^{3+} emission is not surprising because the transitions from E_g to $^2F_{7/2}$ and $^2F_{5/2}$ are fully allowed [21]; in fact Gaft et al. [22] observed the Ce^{3+} emission band at 355 nm with a short decay-time of 30 ns in natural calcite under laser excitation at 266 nm.

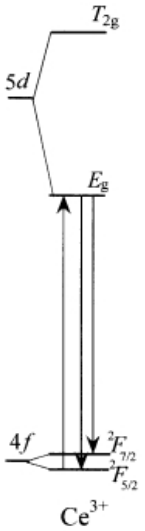

Figure 1-14: Diagram illustrating energy transition of Ce^{3+} in calcite

The violet emission of the radiation-induced center $(CO_3)^{3-}$ is well known in steady-state luminescence spectra of calcite [23] [24]. The problem is that Ce^{3+} also has emission in the UV part of the spectrum. In time-resolved luminescence spectroscopy it is possible to differentiate between these two centers because of the longer decay time of the radiation-induced center. Its luminescence peaking at 403 nm becomes dominant after a delay time of $100 - 200$ ns while emission of Ce^{3+} is already quenched (Figure 1-15 b).

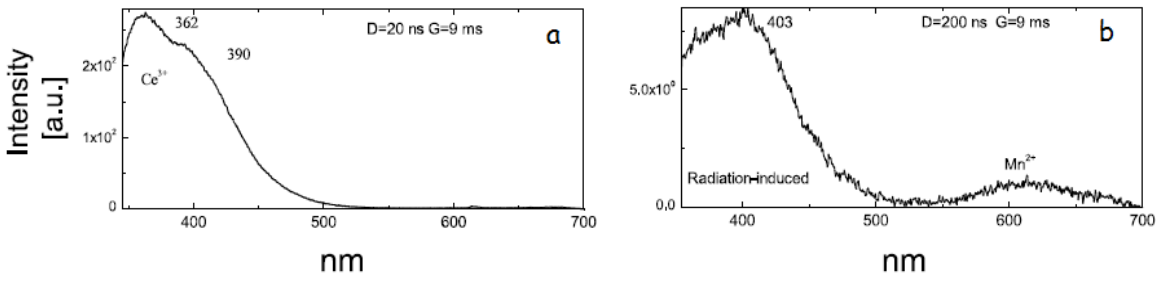

Figure 1-15: Laser-induced time-resolved luminescence spectra of calcite demonstrating Ce^{3+}(a) and radiation-induced centers (b) [22]

Intra-configuration $4f^n \rightarrow 4f^n$ transitions

The number of free ion $4f^n$ levels becomes quite large in the middle of the RE series (Figure 1-16). Thus, especially for the $4f^4$ to $4f^{10}$ electronic configurations, several levels usually form a block of states, in which non-radiative multi-phonon relaxation predominantly occurs. RE ions have the fairly unique property of emitting narrow, weak lines in solid phase in the infrared, visible, and UV part of the spectrum.

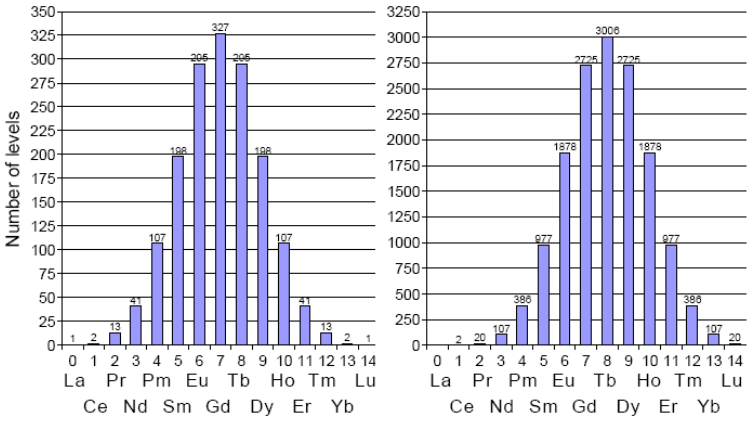

Figure 1-16: Number of free ion $4f^n$ (left) and $4f^{n-1}5d$ (right) evels for trivalent RE ions. Values taken from [14]

Each $^{2S+1}L_J$ level is split into up to $(2J+1)$ sublevels by the crystal field Stark effect, further depending on the local symmetry. The energy levels scheme of trivalent *REE* may be seen in Figure 1-17.

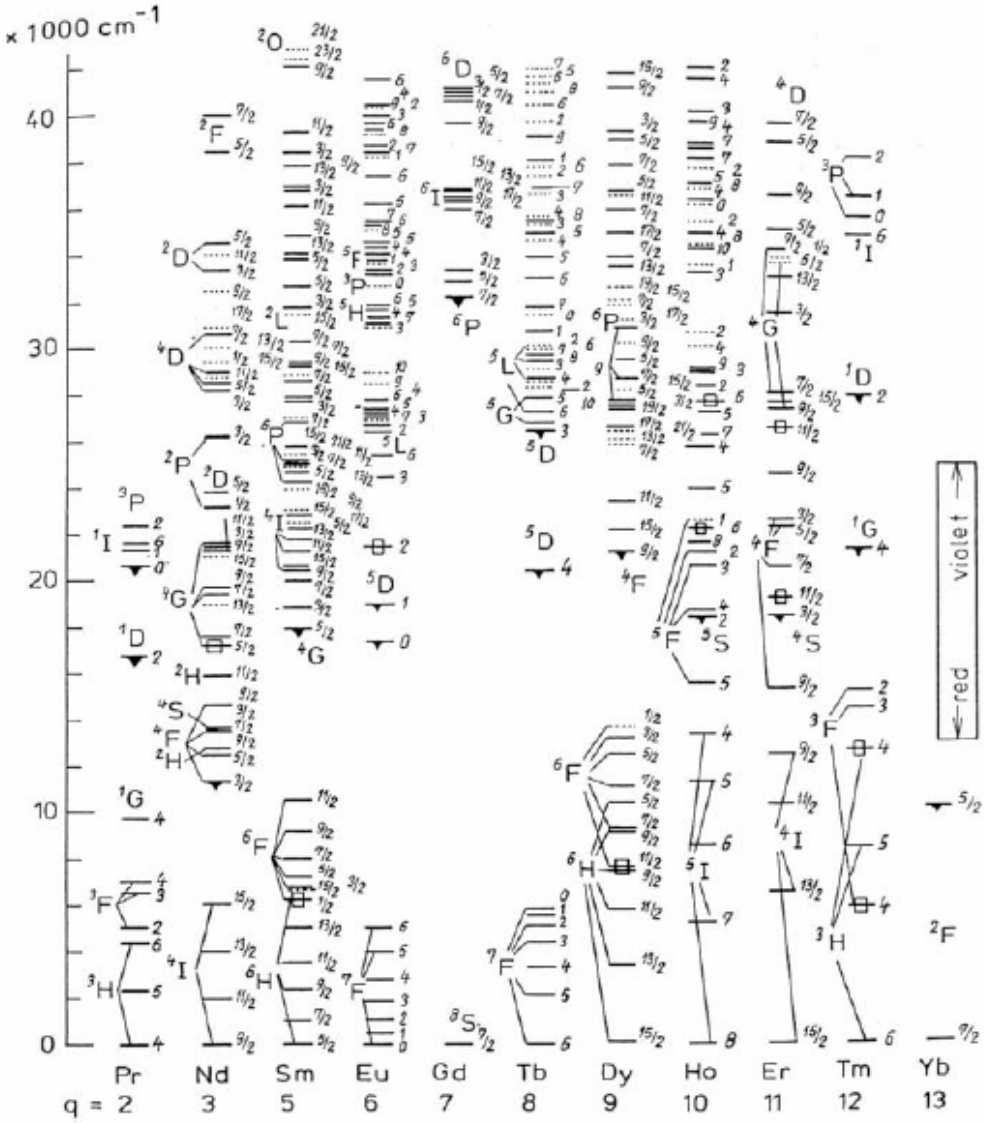

Figure 1-17: Energy levels scheme for trivalent rare-earth elements [22]

For a free ion, electric dipole transitions between states of the same configuration are strictly parity forbidden and the observed spectra of glasses, crystals, or solutions result from non-centrosymmetric interactions that lead to a mixing of states of opposite parity.

One of the most important mechanisms responsible for the mixing is the coupling of states of opposite parity by way of the odd terms in the crystal field expansion of the perturbation potential H_{cf} (Equation 1.14), provided by the crystal environment about

the ion of interest. From perturbative theory, follows

$$|\psi_{mix}\rangle = |\phi_n\rangle - \sum_j \frac{\langle\phi_n| H_{cf}^{odd} |\phi_j\rangle}{E_n - E_j} |\phi_j\rangle \tag{1.15}$$

where j runs on opposite parity states respect n and $|\phi_i\rangle$ are the eigenfunctions expressed in terms of Russell-Saunders states $^{2S+1}L_J$ while E_i are corresponding levels.

This forced electric dipole mechanism was treated in detail for the first time by Judd [11] and after by Judd and ofelt [11][12].

Dysprosium

Dysprosium activated minerals have luminescence in the visible part of the spectrum. The CL (Cathodoluminescence-Spectra) spectra of Dy^{3+} in minerals (in Figure 1-18 Dy^{3+} in Calcite) are mainly characterized by four peaks respectively located at $478 - 487nm$ ($^4F_{9/2} \rightarrow^6 H_{15/2}$), $573 - 586\ nm$ ($^4F_{9/2} \rightarrow^6 H_{13/2}$), $660 - 673\ nm$ ($^4F_{9/2} \rightarrow^6 H_{11/2}$) and $751 - 761\ nm$ ($^4F_{9/2} \rightarrow^6 H_{9/2}$) [25]; usually the second term of them is most intensive in many minerals. All luminescence lines of Dy^{3+} are characterized by decay time of 720 μs [22].

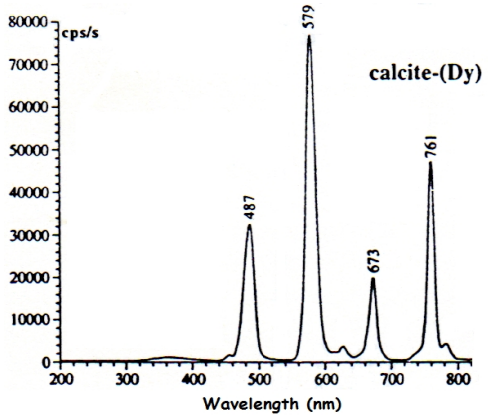

Figure 1-18: Cathodoluminescence Spectra of Dy^{3+} in calcite [25]

Chapter 2

Experimental setup

The scanning electron microscope (SEM) is a type of electron microscope that produces an image of the sample surface by scanning it with a high-energy beam of electrons in a raster scan pattern. The electrons interact with the atoms that make up the sample producing signals that contain information about the sample's surface topography, composition and other properties such as electrical conductivity.

The types of signals produced by an SEM include secondary electrons, back-scattered electrons (BSE), characteristic X-rays, light (cathodoluminescence), specimen current and transmitted electrons. Secondary electron detectors are common in all SEMs, but it is rare that a single machine would have detectors for all possible signals. The signals result from interactions of the electron beam with atoms at or near the surface of the sample. In the most common or standard detection mode, secondary electron imaging or SEI, the SEM can produce very high-resolution images of a sample surface, revealing details about less than 1 to 5 nm in size. Due to the very narrow electron beam, SEM micrographs have a large depth of field yielding a characteristic three-dimensional appearance useful for understanding the surface structure of a sample. A wide range of magnifications is possible, from about 10 times (about equivalent to that of a powerful hand-lens) to more than 500000 times, about 250 times the magnification limit of the best light microscopes. Back-scattered electrons (BSE) are beam electrons that are reflected from the sample by elastic scattering. BSE are often used in analytical SEM along with the spectra

made from the characteristic X-rays. Because the intensity of the BSE signal is strongly related to the atomic number (Z) of the specimen, BSE images can provide information about the distribution of different elements in the sample. For the same reason, BSE imaging can image colloidal gold immuno-labels of 5 or 10 nm diameter which would otherwise be difficult or impossible to detect in secondary electron images in biological specimens. Characteristic X-rays are emitted when the electron beam removes an inner shell electron from the sample, causing a higher energy electron to fill the shell and release energy. These characteristic X-rays are used to identify the composition and measure the abundance of elements in the sample.

The term Cathodoluminescence (CL) designates the luminescence induced by electron bombardment.

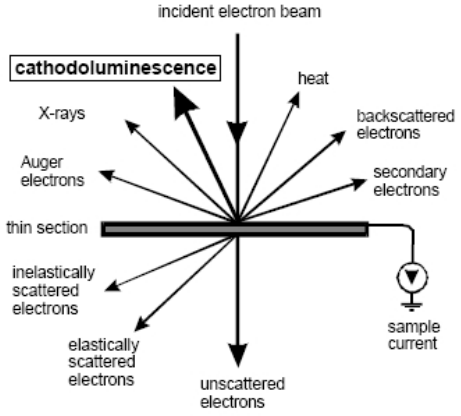

Figure 2-1: Schematic representation of processes resulting from electron bombardment.

The interaction of the electron beam with the sample gives rise to a number of effects: the emission of secondary electrons (SE), back-scattering of electrons (BSE), electron absorption ("sample current"), characteristic X-ray, and CL emission (Figure 2-1).

Most energy of the beam is converted into heat. The penetration depth of electrons and accordingly, the excitation depth depends on the electron beam energy and is in the range of $2 - 10\ \mu m$ [26].

The scanning electron microprobe (SEM) utilises a scanned electron beam with a small spot size normally around few microns in diameter. By scanning the electrons,

by driving the the X-Y positions of a focused beam on the specimen, it is possible to obtain a magnified map of the CL of the specimen. The SEM-CL offers advantages over the conventional (optical) CL microscopy for CL studies [27][28]. The main advantage is a larger spatial resolution, roughly about $1\mu m^2$. Other advantages are the higher magnification, the capability of combining CL and SEM investigations like back scattered electron (BSE) imaging and microanalytical analysis (EDX) on the same area.

2.1 SEM-CL Apparatus

In our case, CL measurements have been performed using a Cambridge Stereoscan 360 SEM equipped with a Horiba Jobin Yvon VS140 UV-VIS spectrometer (Figure 2-2), spectral resolution of $\sim 1\ nm$ and a 1200 l/mm plane diffraction grating blazed at 546 nm.

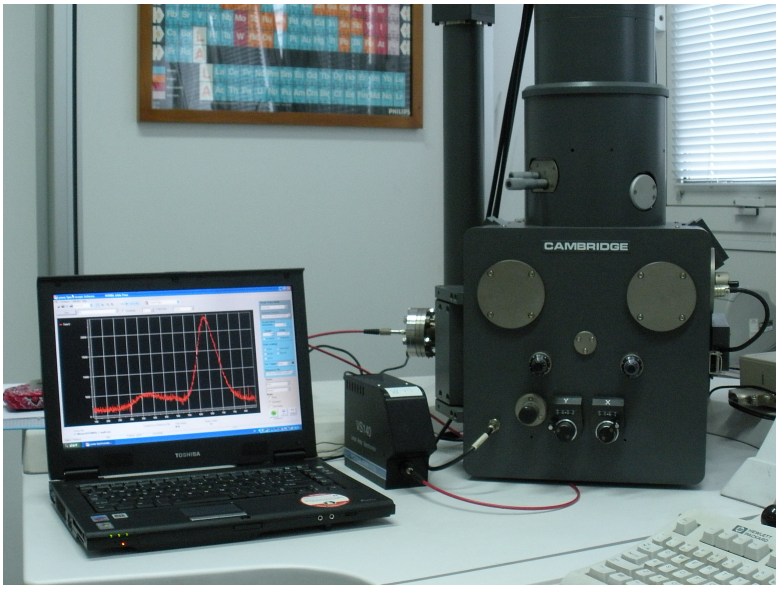

Figure 2-2: Cambridge Stereoscan 360 SEM equipped with a Horiba Jobin Yvon VS140

The SEM apparatus has the advantage of supplying an energetic electron beam (up to 40 keV). The idea is then to modify the original SEM configuration by adding a CL apparatus so that one can obtain, simultaneously on the same spot, luminescence

spectra, SEM-BSE images, and also the possibility of chemical analysis by EDX (Energy Dispersion X-ray) protocols. Figure 2-3 shows in details the modification introduced in the old apparatus in order to achieve the previous mentioned advantages.

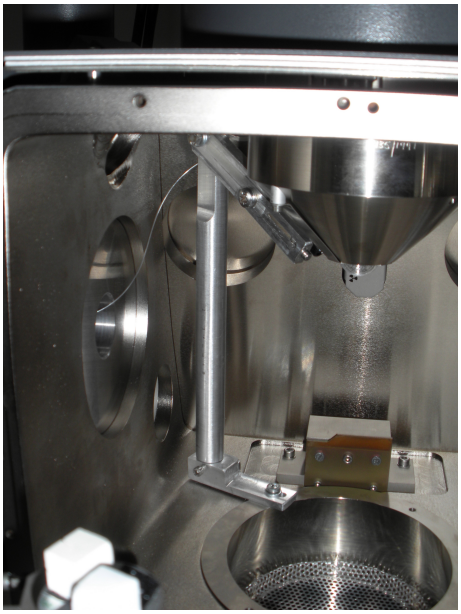

Figure 2-3: Our modified Cambridge Stereoscan 360 SEM

On a mechanical support fixed inside the chamber, we have anchored a sliding rail. On this sliding rail a small lens was fixed (Figure 2-4), allowing to change the position of the lens through a series of screws.

Figure 2-4: The lens that collects the luminescence signal

The mechanical system has been designed and fabricated by using appropriate vacuum-compatible materials and having in mind that the final lens position needed to be directed

in the same area where the SEM beam is normally pointed for the usual investigations. The lens, of course, has been introduced to collect the luminescence signal genearated by the electron beam to achieve the CL signal. The signal is focused in the lens and transported out of the chamber by means of an optical fiber, and the luminescence intensity is then analyzed in the Horiba Jobin Yvon VS140 UV-VIS spectrometer. The signal transport is obtained without breaking the chamber vacuum by modifying a chamber flange in order to connect the portion of the optical fiber allocated inside the vacuum side with the portion outside the chamber connected to the spectrometer. All the mentioned part (lens, optical fiber, feed through flange) have been chosen to be compatible with the spectrometer wavelength range ($200 - 1100\ nm$).

By using a laser , the lens has been fixed in a way that it looks to the same area where the SEM electron beam is directed (normally at a working distance of 19 mm from the beam exit). This allow to the lens the collection of the CL signal coming from the electron beam spot (Figure 2-5). All the relative distances have been chosen in order to obtain a good compromise between a higher CL signal intensity, a good SEM-BSE image quality and the possibility to insert in the chamber samples of different sizes.

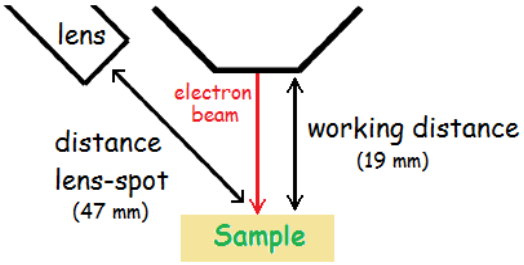

Figure 2-5: Schematic diagram of the lens-beam geometry

Then the lens focus has been finely determined by measuring the intensity signal collected from a small spot emitting source. The measured intensities are reported in Figure 2-6.

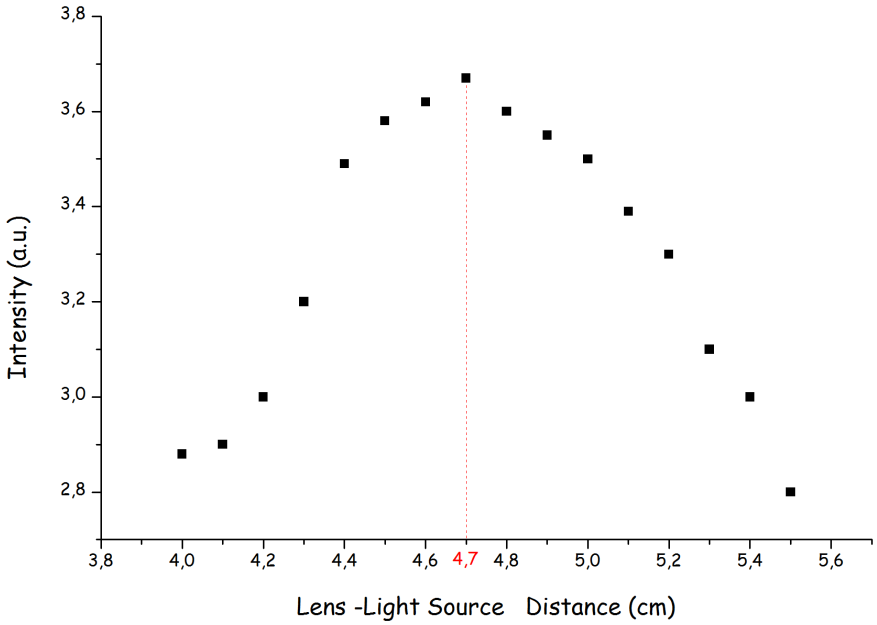

Figure 2-6: Determination of the lens focus

As it can be seen from the Figure 2-6 the best signal is obtained at a distance of 4.7 *cm*. All the distances have been the fixed and the CL signal has been monitored under vacuum conditions in different configurations (regarding beam energy, spot size, beam current, sweeping frequency, probing area etc.) and using different materials as samples. The signal has been processed in the spectrometer which is driven by a data acquisition system controlled through a computer. Once the system has been tested in its final configuration, a series of measurements to establish the operation protocol has been performed and compared with the literature and then the same protocol has been applied to perfom research experiments. The results are reported in the next chapter.

Chapter 3

Experimental results

In this section we report our measurements which are carried out by implementing on various samples the CL protocol as established in the previous section. The spectra so obtained can be distinguished essentially in two parts. In the first part we present the measurements on well known materials, where "well known" in this case means from the point of view of luminescence properties of such materials. Such measurements have been executed to check the performances and the efficiency of our apparatus with well established values in literature, going to compare our measurements with referenced values used as standards. In the second part we show all the new measurements made on materials for which luminescence data are scarce or even absent. Moreover, from the theory exposed in chapter 1, we try to give some new assignation to CL peaks of some materials and we will use the Mn^{2+} luminescence emission in calcite to perform a calibration of our instrument by means of data acquired on the same materials using Laser-Induced Coupled Plasma analysis, which is a technique very sensible to traces of elements (up to $10 - 100$ *ppb*).

3.1 Corundum-Ruby

One of the most studied compound in terms of luminescence properties is the Corundum, so that we first refer our CL results to such material since it is easy to find a comparison with results disseminated in literature. Moreover since the Corundum luminescence peak at 694 nm has a well defined narrow emission, this allows us also to check the response of our apparatus in terms of wavelength.

Corundum is a crystalline form of aluminum oxide (Al_2O_3) with traces of iron, titanium and chromium. It is one of the naturally clear transparent materials, but can have different colors when different impurities are present. Transparent specimens are used as gems, called ruby if red, while all other colors are called sapphire.

Corundum has a trigonal structure. The oxygen ions are arranged in approximately hexagonal closed packing. Between the oxygen layers there are sites for cations octahedrally coordinated by six oxygen ions, but in corundum only two-thirds of the available positions are filled. Groups of three oxygen ions form a common face of two octahedral neighboring and thus the groups are linked to a pair of Al ions.

The main colored varieties are ruby (red) and sapphire (blue). The corresponding color centers can be present in different quantitative and qualitative proportions with resulting varieties of colors (up to 2000 different tints). The main color center in ruby is an impurity of Cr (up to 4%). The ion Cr^{3+} generates two strong absorption bands in the visible part of the spectrum, which explain the red color. Different tints of red, which influence the commercial value strongly, are connected with impurities of Fe^{3+} and V^{3+}. Under UV excitation, ruby may exhibit the red luminescence of Cr^{3+}, which makes the red color of ruby stronger under sun illumination.

3.1.1 Tanabe Sugano diagram of Cr^{3+}

From a theoretical point of view the narrow peak in the ruby due to Cr^{3+} can be explained in the following, considering the Tanabe Sugano diagram of Cr^{3+}.

The most important free ion states are ^4F ground level and excited ^2G level. In an octahedral field, the ^4F level splits into the $^4A_{2g}$ ground state and the excited $^4T_{2g}(F)$ and $^4T_{1g}(F)$ states.

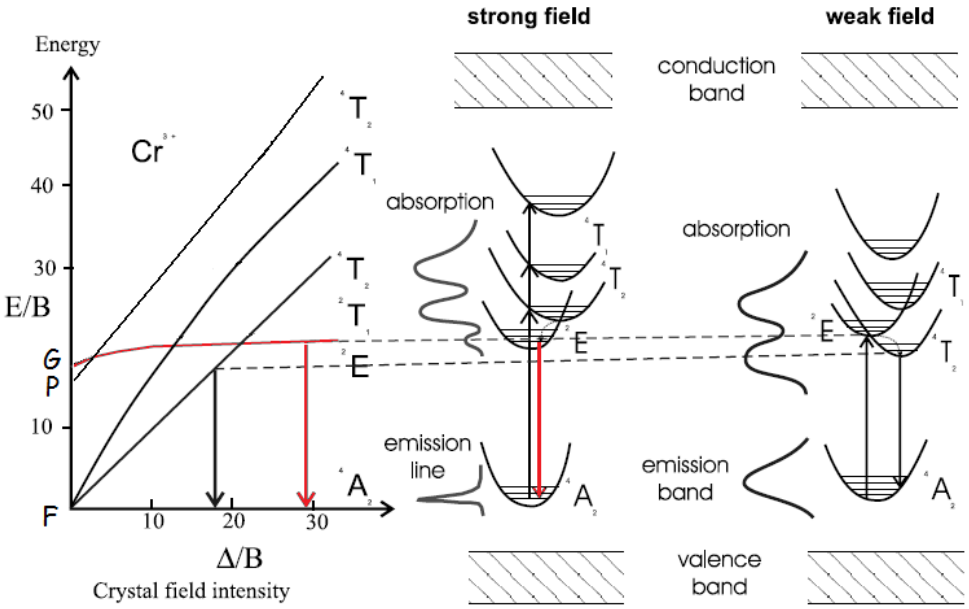

Figure 3-1: Tanabe Sugano diagram of Cr^{3+} [22]

The spin allowed transitions that could therefore be used to populate the excited states directly correspond to $^4A_{2g}(F) \rightarrow {}^4T_{2g}(F)$ and $^4A_{2g}(F) \rightarrow {}^4T_{1g}(F)$. Mostly Cr^{3+} appears in minerals as a trace constituent substituting for Al^{3+} in six-fold coordination. As such, the larger Cr^{3+} ion is placed in a site with small metal-ligand distances and where the crystal field is large, typically $16500 - 17500\ cm^{-1}$. As may be seen in Figure 3-1, if the crystal field is sufficiently strong to make the doublet state the lowest energy excited state, there will be a red luminescence. Because the doublet state belongs to the same orbital configuration as the ground state, the Stokes shift and Condon offset will be small (Figure 1-8 in section 1.4). As a result, the line width of emission is narrow and a considerable amount of phonon fine structure is observed even at room

temperature. Such a transition is forbidden by symmetry and spin selection rules (red downward arrow in Figure 3-1) and the decay time is usually very long (several ms). At weaker crystal fields, a strong broad band ${}^4A_{2g}(F) \rightarrow {}^4T_{2g}(F)$ transition appears, which is only symmetry forbidden and has a much shorter decay time.

Ruby is a high crystal field material and thus the ${}^4T_{2g}$ state lies above the ${}^2E_g$ level. Pumping is accomplished by a spin-allowed transition into the ${}^4T$ state, while emission occurs from the ${}^2E_g$ level without vibrational broadening and almost all excited states can be converted into laser action.

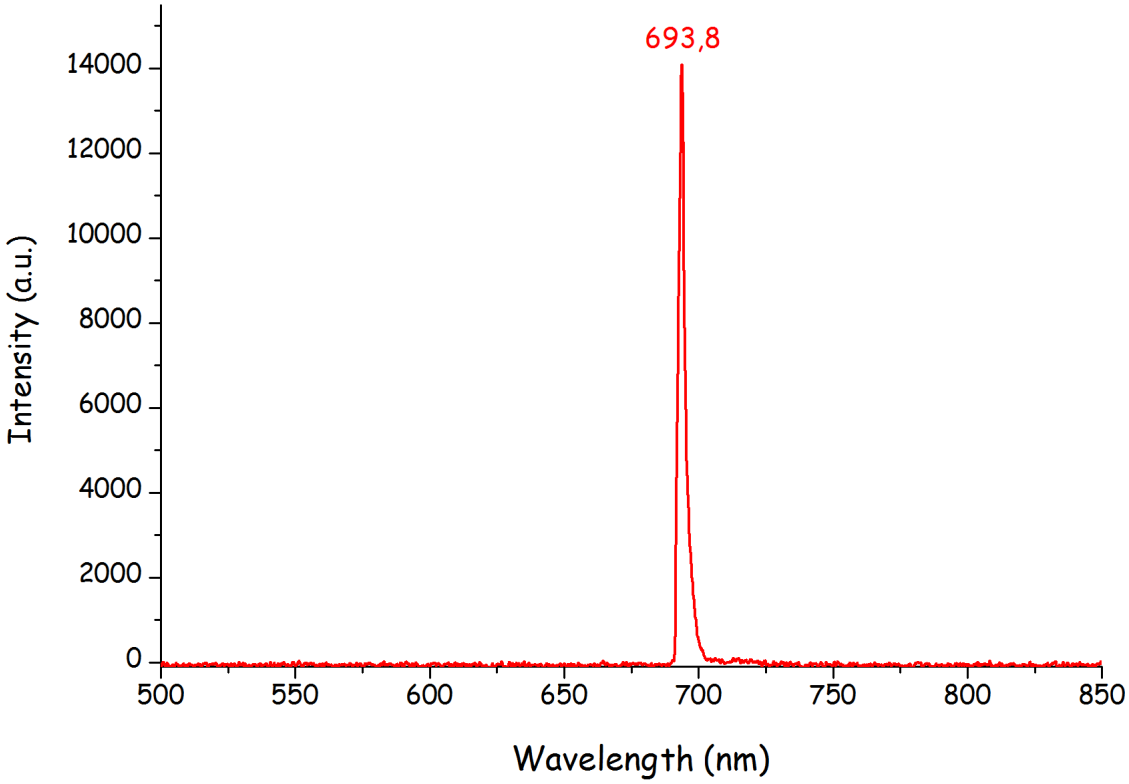

Figure 3-2: CL spectrum of Ruby as obtained in our apparatus

The obtained CL spectrum (Figure 3-2), peaking at $693,8\ nm$, shows ${}^2E_g(G) \rightarrow {}^4A_{2g}(F)$ transitions. Due to the resolution of our instrument we obtain a convolution of the two mentioned transitions, but the peak position in terms of wavelength is in perfect agreement with what can be found in literature [22].

3.2 Mn^{2+} in different lattices

Additional measurements achieved to check the functionality of our apparatus have been carried on Mn. According to what has been discussed in section 1.6, different spectra related to Mn^{2+} transitions in different crystal are shown as measured in our new instrument.

In Figure 3-3 is reported a typical CL spectrum as registered bombarding a quartz sample.

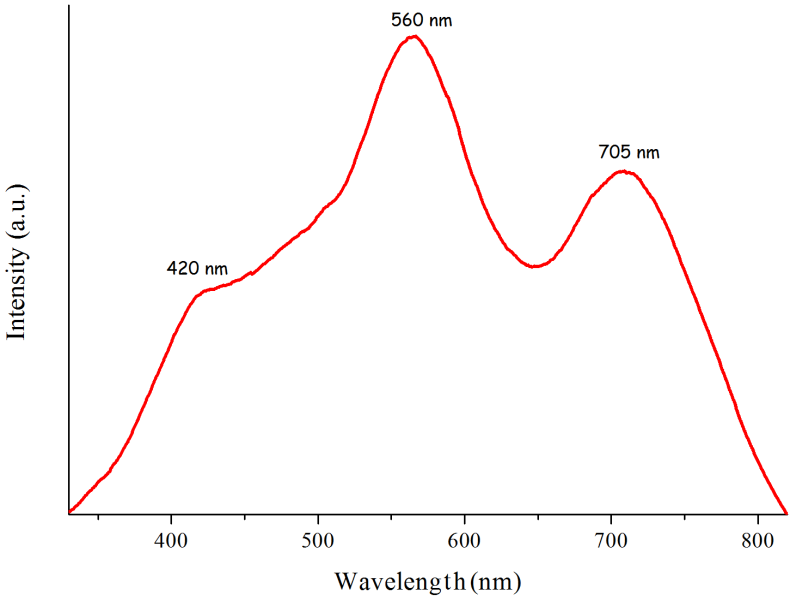

Figure 3-3: CL Spectra of quartz. The peaks related to Mn^{2+} and to Fe^{3+} are repectively at 560 nm and at 705 nm. The shoulder raising at 420 nm is related to intrinsic defects of quartz [29]

Changes in coordination, such as from octahedral to tetrahedral, produce a considerable change in Dq. The tetrahedral Dq value is smaller (Figure 1-4) and the energy of the Mn^{2+} transitions increases (Figure 1-9). This creates a shift toward shorter wavelengths. Octahedral Mn^{2+} coordination in calcite thus has a red-orange emission near to 620 nm (Figure 3-4), while the analogous transition for Mn^{2+} in quartz yields yellow-green emission near to 560 nm [30], as obtained in our measurements of Figure 3-3.

Luminescence of Fe^{3+} may be considered from the same diagram as in the case of Mn^{2+} emission, because it also has d^5 configuration. Nevertheless, because of the large value of crystal field (Equation 1.10), the emission is shifted into the deep red when Fe^{3+} is present on tetrahedral sites [31] at 705 nm. The presence of Mn and Fe was confirmed by additional XRF analysis (obtaining for $Mn \sim 100$ ppm and for $Fe \sim 300$ ppm).

In Figure 3-4 are reported typical Mn^{2+} spectra in calcite and dolomite.

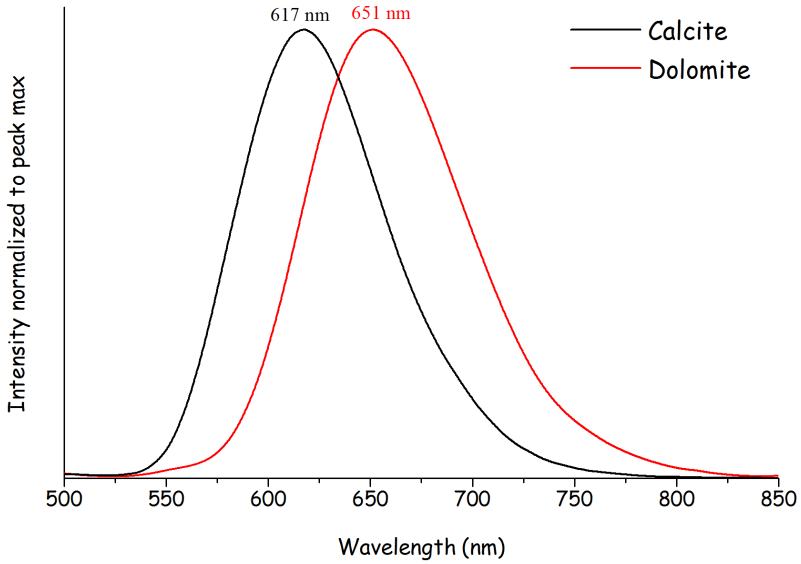

Figure 3-4: Measured CL spectra of Mn^{2+} in Calcite e Dolomite. The peak of Mn^{2+} at 651 nm in dolomite is in agreement with [32]

The preference of Mn^{2+} for the smaller Mg site in most dolomites is now well-documented experimentally, by both luminescence and electron spin resonance (ESR) measurements. It was found that in sedimentary dolomites such preference of Mn^{2+} in Mg/Ca sites reflects the ratio of 4 : 1, whereas, in some hydrothermally altered dolomites it was much higher [33]. Such ratios for the preference of Mn^{2+} in Mg/Ca site population have been found also by other researchers [34].

The obvious question is whether the usual strong preference of Mn^{2+} for the Mg sites in dolomite ($CaMgC_2O_6$) is to be expected on theoretical grounds. The distribution of the Mn^{2+} in Mg and Ca sites is related to their residence time during crystal growth at roughly 650 $°C$. The residence time in a particular site is likely to be related to the binding

energy E by a Boltzmann factor $exp(-E/kT)$. If the potential energy curve is assumed to be parabolic then E will depend on the square of the difference in cation-anion distances. However, the size of the constant of proportionality which determines the "width" or curvature of the parabolic potential curve is not known. Furthermore, the precise form of the potentials energy vs. cation-anion distance curve may not be parabolic for Mn^{2+} octahedrally co-ordinated by oxygen ligands in carbonates. Nevertheless, the curve is likely to have a roughly similar shape to a *Morse* potential and is shown schematically in Figure 3-5.

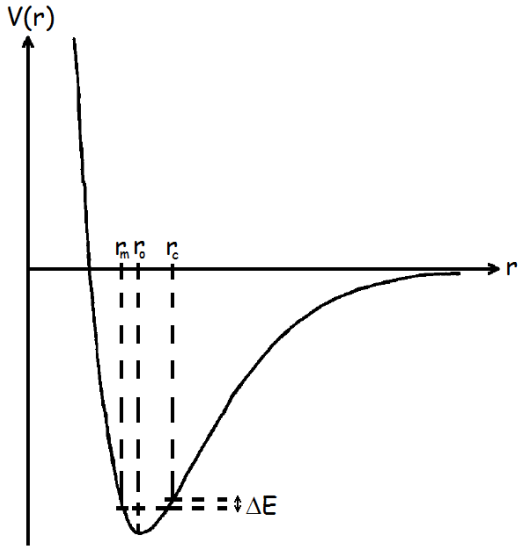

Figure 3-5: Schematic diagram of the probable potential energy curve $V(r)$ vs. r (cation-anion distance) curve for Mn^{2+} in octahedral coordination by oxygen ligands in carbonates: r_0 is the cation-anion distance for minimum energy and corresponds approximately to that which exists in rhodochrosite $MnCO_3$, r_m and r_c are the cation-anion distances for Mn^{2+} in the Mg site and Ca site respectively in dolomite (see Table 1.2). ΔE is the energy difference between Mn^{2+} in a Ca site and that in a Mg site in dolomite [17]

Here the energy difference ΔE is that between an Mn^{2+} ion in a magnesium site and Mn^{2+} in a calcium site. The population ratio is then $exp(\Delta E/kT)$ where T (K) is the absolute temperature of formation or that at which appreciable ion diffusion has taken place. If, for example, $\Delta E = 2kT$ the Mg/Ca site population ratio would be about 7 and even at 650 $°C$, $2kT$ is only around 0.15 eV.

The effect of a small variation in the cation-anion distances can be readily seen. For example, high pressure would tend to reduce cation-anion distances and thereby decrease ΔE, resulting in a smaller Mg/Ca population ratio at a particular temperature (T).

The effect of the temperature of formation on Mn^{2+} distribution is rather more difficult to predict since both ΔE and kT would decrease with decreasing temperature. Although experimentally the most common Mg/Ca site population ratio appears to be about 5, there can be a very large variation: the difference in lattice energy between placing Mn^{2+} ions in Mg sites and placing them in Ca sites must be relatively small and that differences in conditions of formation and/or subsequent alteration can cause the balance between Mg and Ca site population to be tilted one way or the other.

3.3 Marbles

Pure white marble has been considered a valuable ornamental and architectural material since ancient times. Many scientific techniques have been used to create an extensive data base of "finger-prints" characterizing white marbles from the major classical quarries. However, determining the provenance of white marbles is a difficult task due to their similarity in physical and chemical parameters. Three techniques (petrography, cathodoluminescence and stable C and O isotopes) have been used to characterize white marbles from the ancient quarries of the Iberian Peninsula [35].

We used marbles only as standards, in order to correlate CL signal with manganese concentration [36], determined using a Laser Ablation microsampler coupled to an Inductively Coupled Plasma Mass Spectrometer (LA ICP-MS).

The samples investigated are Carrara marbles; this kind of marble is metamorphic rock that outcrops extensively in the Apuan Alps (Tuscany, Italy) and is a granular calcite-made metamorphic product, which originates from pelagic limestone.

Samples come from four different quarries of the same district (Carrara), and for each quarry we have investigated three samples, with exactly three types of cut:

- V: verso

- S: secondo

- C: contro.

The quarries are summarized as follows:

- Cava Calocara, Torano-Carrara (CAL);

- Cava Crestola, Torano-Carrara (CRE);

- Cava Focolaccia, Massa (FOC);

- Cava Romana, Massa (ROM).

All samples are cylinders of 3 cm in diameter and 1 cm in height, and to prevent the build-up of electric charge, were coated with carbon.

The operative SEM-CL parameters are:

- acquisition time: 40 s;

- scanning area: 2.7 mm^2;

- scannning frequency: 12.5 Hz;

- accelerating voltage: 20 kV;

- emission current: 6 μA.

The choice of the scanning area is related to the need to map the entire surface of the sample. Scanning area and acquisition time chosen are a good compromise between CL signal and the number of tests to be performed on the same sample.Figure 3-6 shows the CL intensity vs wavelength at different scannning frequency of a ROM V sample with 60 s of acquisition time, 2.7 mm^2 for the scanning area, 20 kV for the accelerating voltage and 6 μA for the emission current.

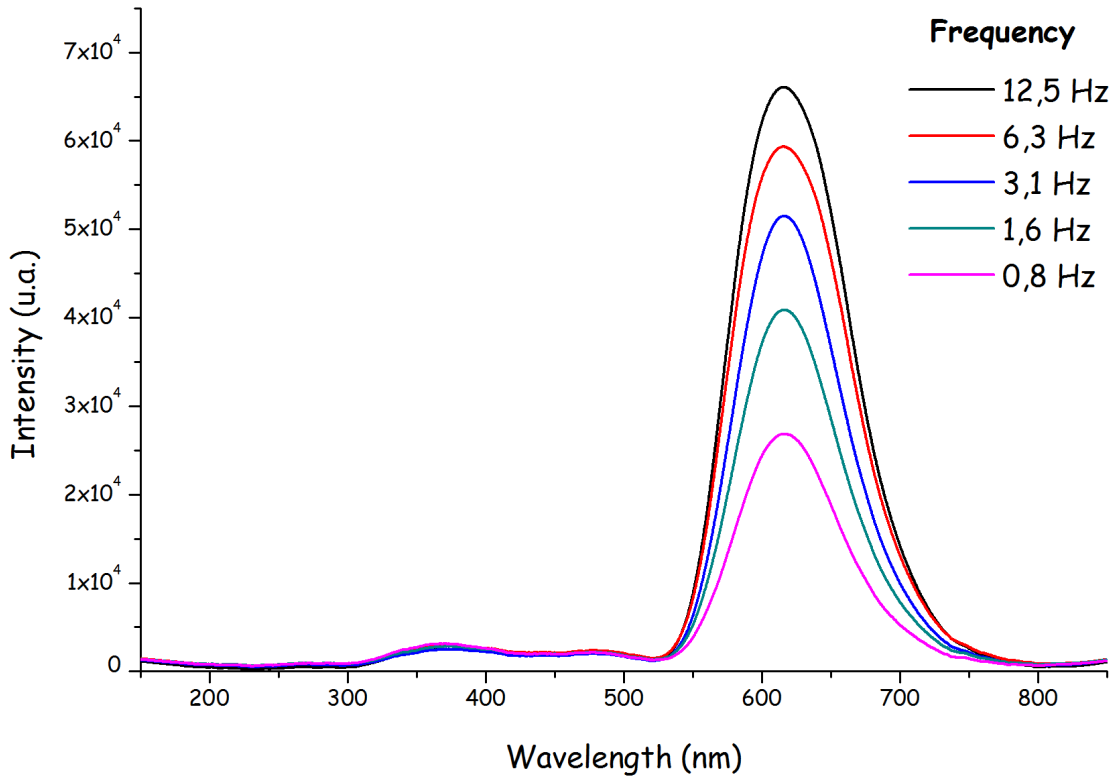

Figure 3-6: CL intensity vs wavelength for different scannning frequency of a ROM V sample with 60 s of acquisition time, 2.7 mm^2 for the scanning area, 20 kV for the accelerating voltage and 6 A for the emission current

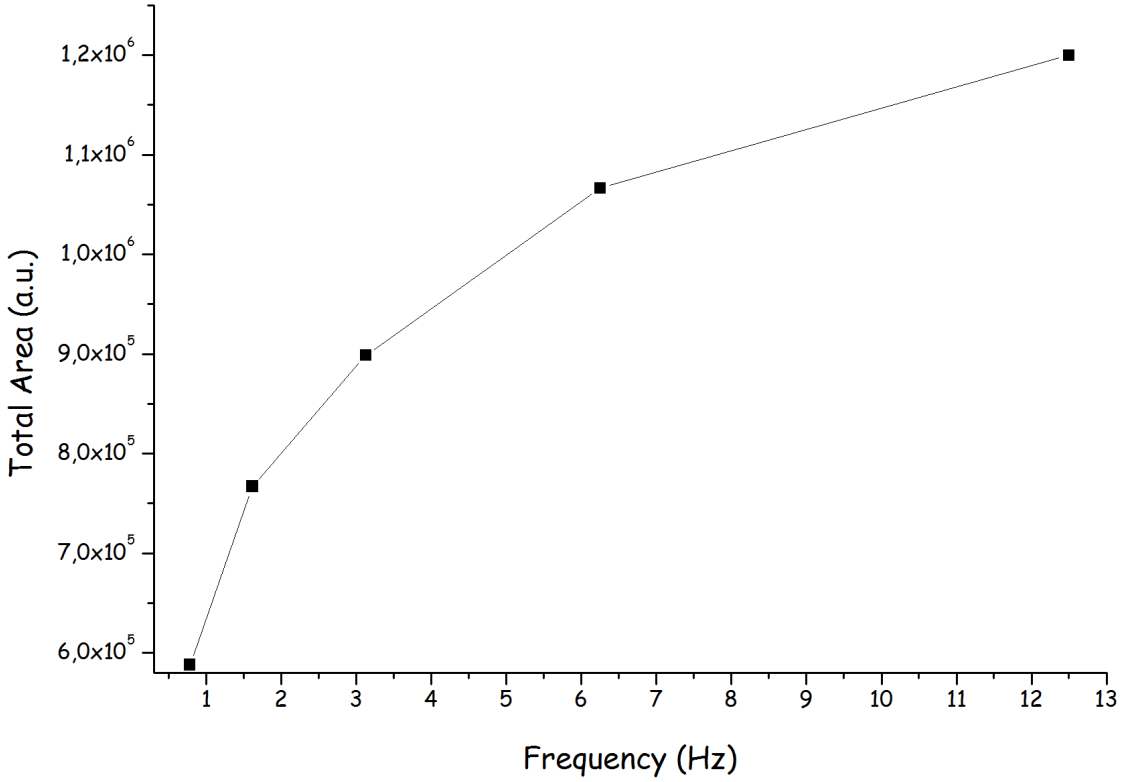

Figure 3-7: CL spectra, integrated over the wavelength, versus scannning frequency

Figure 3-7 shows CL spectra, integrated over the wavelength, versus scannning frequency.

Because the CL signal increases with the scannning frequency, the operating frequency has been chosen in order to enhance the luminescence signal, so that in our measurements we assume a scannning frequency of 12.5 Hz. The dependence on scannning frequency is not linear because the long decay times of Mn^{2+} luminescence is the order of 10 ms [21], and then as the frequency is higher the available time for the decay is reduced. For the same sample, Figure 3-8 shows integrals of CL spectra versus emission current at four different accelerating voltages: 14, 20, 25 and 30 kV.

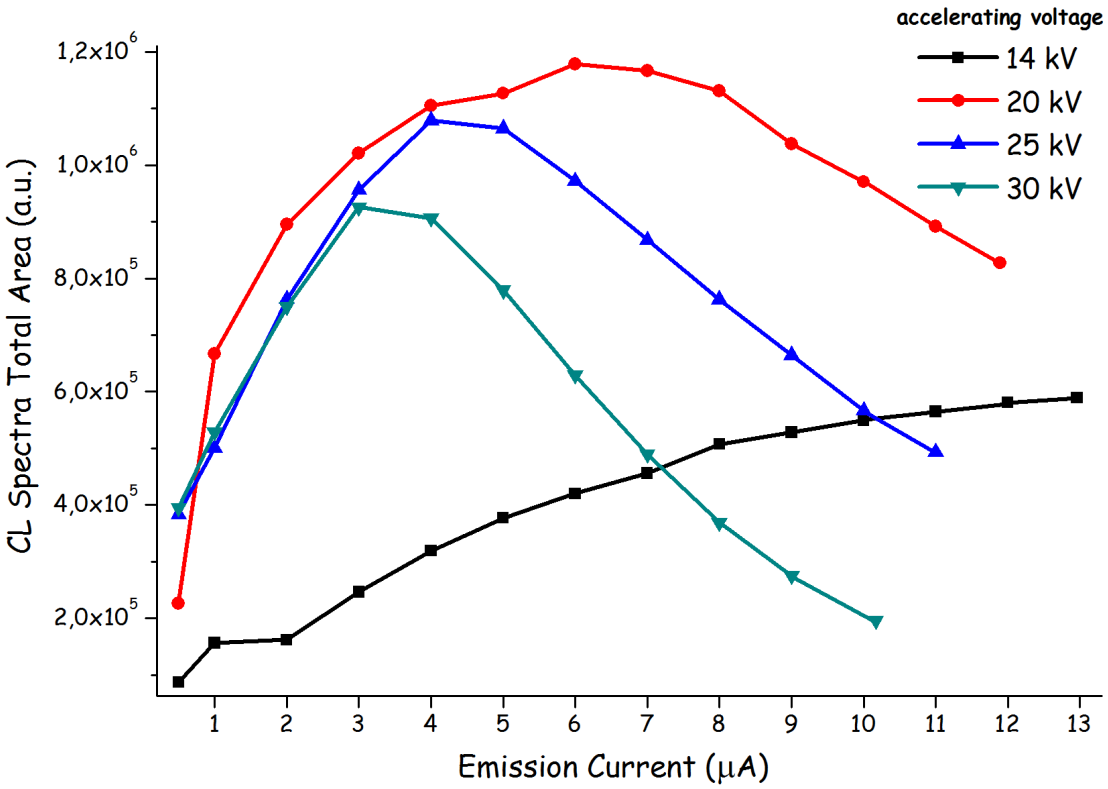

Figure 3-8: Integrals of CL spectra of a ROM V sample versus emission current at four different accelerating voltages: 14, 20, 25 and 30 kV

From the figure it is clear that, to maximize the signal, we use 20 kV for the accelerating voltage and 6 A for the emission current. Figure 3-9 shows CL intensity of all marble samples vs wavelength, while Figure 3-10 shows the same shows CL intensity but normalized to their maximum intensities.

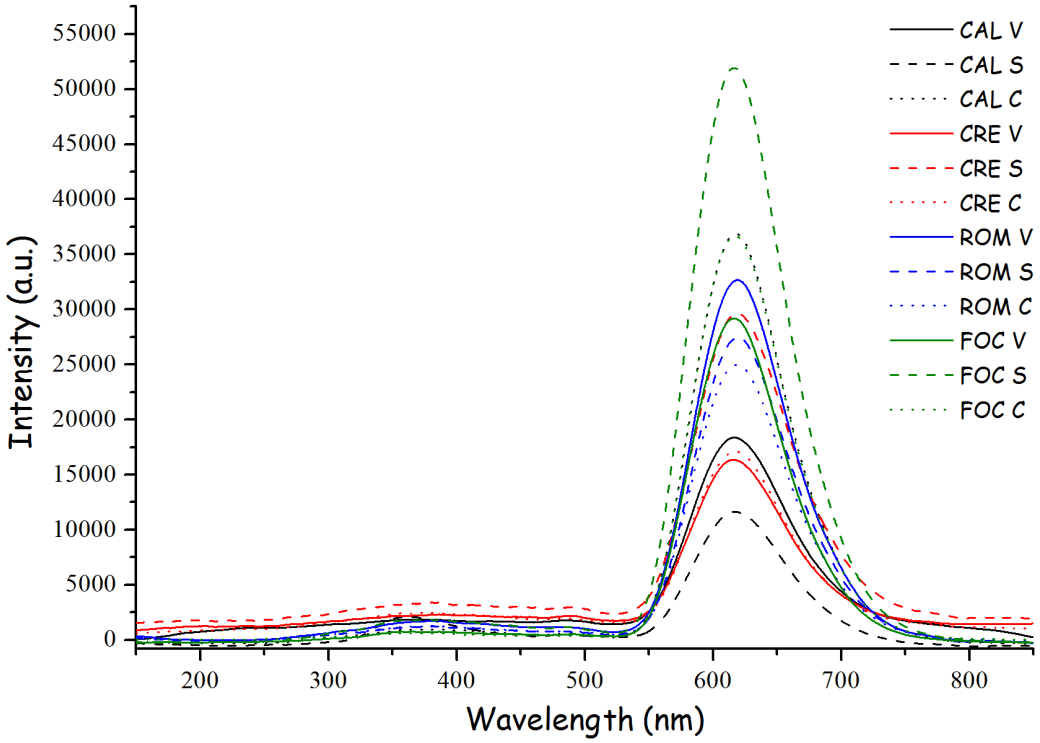

Figure 3-9: CL intensity of all marble samples

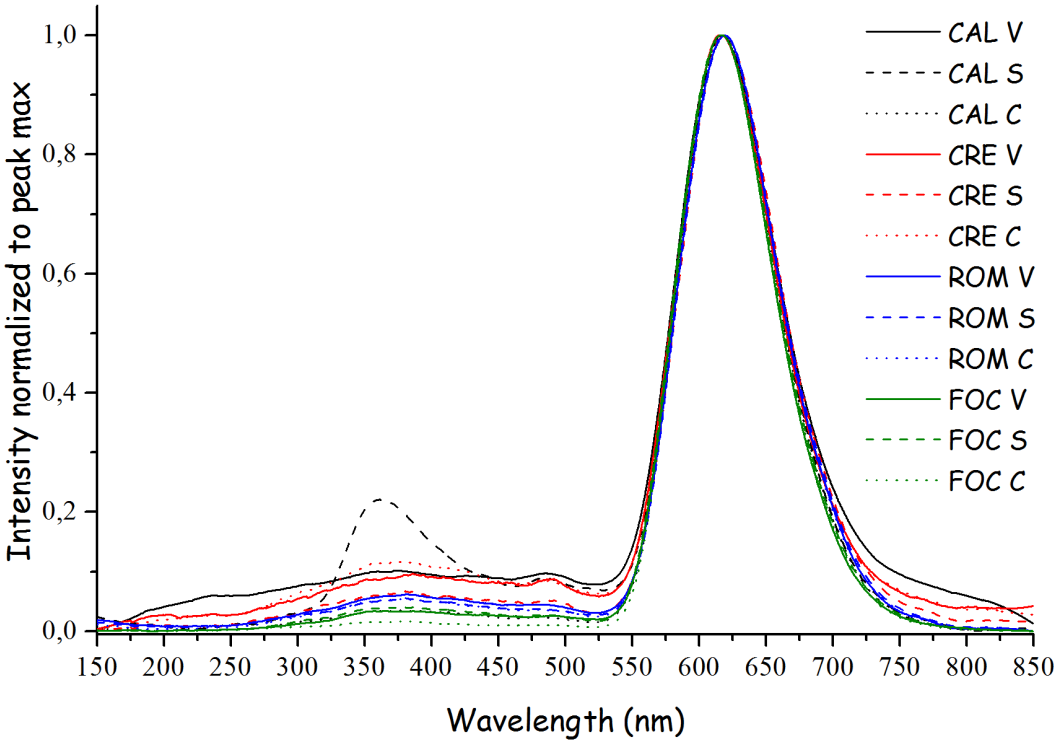

Figure 3-10: CL intensity of all marble samples normalized to their maximum intensities

The interpretation of peaks lying in the range $250 - 550\ nm$ is quite difficult. In a first glance one is tempted to assign the peak at 350 nm to Ce^{3+}. Figure 3-11 shows in fact that the Ce^{3+} peaks at 350 nm and 363 nm, and the Tm^{3+} peak (at 363 nm) are close to the lattice emissions of the calcite (363 nm and 380 nm) as indicated by Pagel et al. [25].

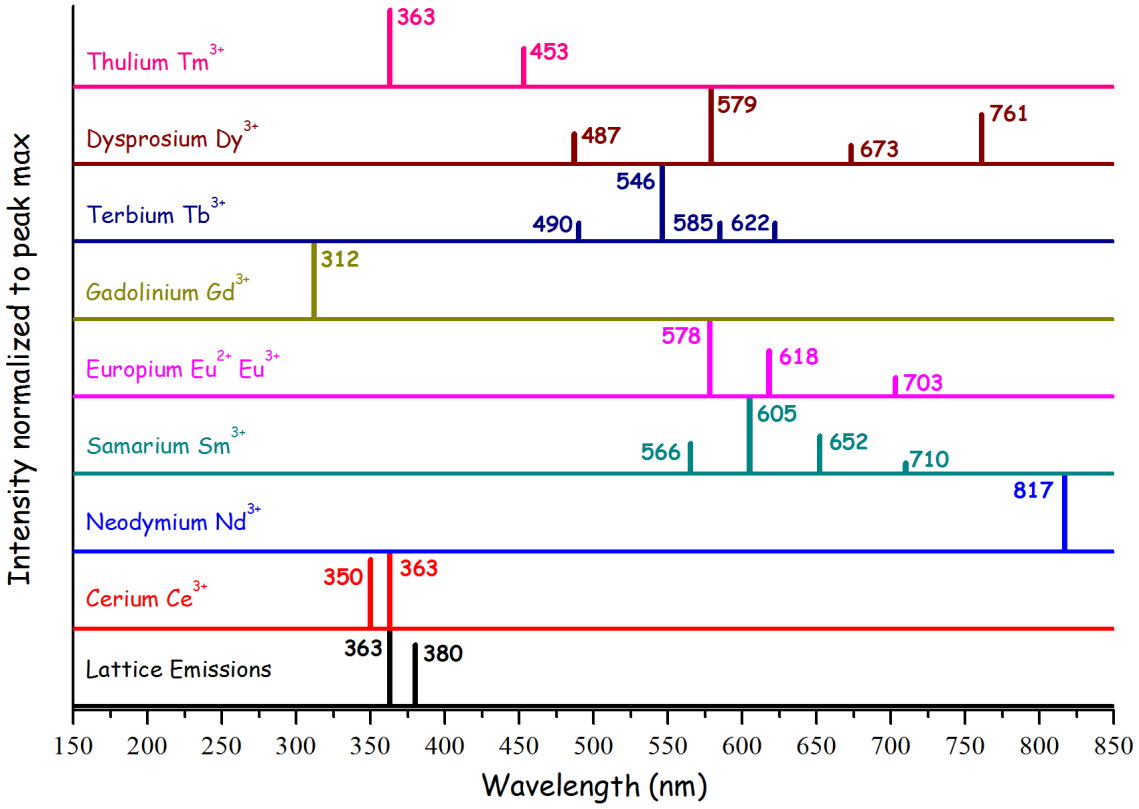

Figure 3-11: Calcite CL peaks attributed to lattice emissions and REE [25]

In the spectrum we can also observe other "intrinsic peaks" in the range from 450 nm to 500 nm. It was shown that the intensities of all intrinsic peaks remain constant during the electron bombardment [37].

In order to bring some light in such attributions we performed LASER-ICP analysis on all the samples. Table 3.1 shows the concentrations of elements sensible to the CL technique as obtained by

Samples	Concentration																	
	ppm																	
	Mg	Mn	Ca	Fe	Ce	Pr	Nd	Sm	Eu	Gd	Tb	Dy	Ho	Er	Tm	Pb
CAL V	10853	43	675535	532	10,53	1,66	6,85	1,09	0,29	1,06	0,13	1,13	0,25	0,51	0,07	1,12
CAL S	9577	18	676250	256	1,82	0,34	1,80	0,26	0,14	0,10	0,05	0,29	0,14	0,39	0,00	1,57
CAL C	241264	169	680395	788	0,51	0,09	0,47	0,00	0,00	0,11	0,04	0,00	0,04	0,00	0,00	1,02
CRE V	9148	23	683719	228	2,74	0,86	4,30	0,97	0,26	1,15	0,15	1,36	0,26	0,74	0,10	1,84
CRE S	13473	39	676286	989	11,47	1,99	8,80	1,84	0,45	1,72	0,28	1,99	0,37	1,04	0,16	3,27
CRE C	9366	23	685148	191	2,28	0,42	1,85	0,35	0,03	0,46	0,05	0,49	0,09	0,33	0,03	2,23
ROM V	7784	41	677144	61	0,39	0,02	0,17	0,21	0,01	0,04	0,02	0,14	0,01	0,03	0,02	0,89
ROM S	8880	49	678752	92	0,25	0,06	0,31	0,11	0,00	0,00	0,02	0,07	0,02	0,00	0,00	0,26
ROM C	9854	50	679645	0	0,34	0,04	0,21	0,02	0,00	0,03	0,00	0,00	0,00	0,00	0,00	1,87
FOC V	5195	90	688293	70	1,71	0,34	1,77	0,16	0,05	0,27	0,10	0,58	0,14	0,59	0,04	1,36
FOC S	5343	71	687042	126	2,36	0,54	2,32	0,37	0,08	0,69	0,09	0,71	0,16	0,54	0,10	0,96
FOC C	4859	106	694511	106	1,98	0,45	2,07	0,33	0,04	0,47	0,06	0,64	0,13	0,51	0,01	2,49

Table 3.1: Element concentration obtained by LASER-ICP analysis

LASER-ICP analysis. From this table it can be seen, for example, that the Ce concentration in the CAL S sample is even smaller than the concentration of the same element in the CAL V sample. So it appears difficult to attribute the peak at 363 nm to Ce, since this peak should be exibit a higer intensity in the CAL V sample with respect to the CAL S sample, while is this last sample which exibits a higer intensity at 363 nm. So that is probably more appropriate the attribution of such peaks to the intrinsic defects. In fact if we look to the CL spectra of pure calcite, where Ce is certainly not present, we have also emission in the ranges $360-390$ nm and $440-500$ nm as measured by Habermann et al. [37], so that we are more favourable in attributing such peaks to the intrinsic defects.

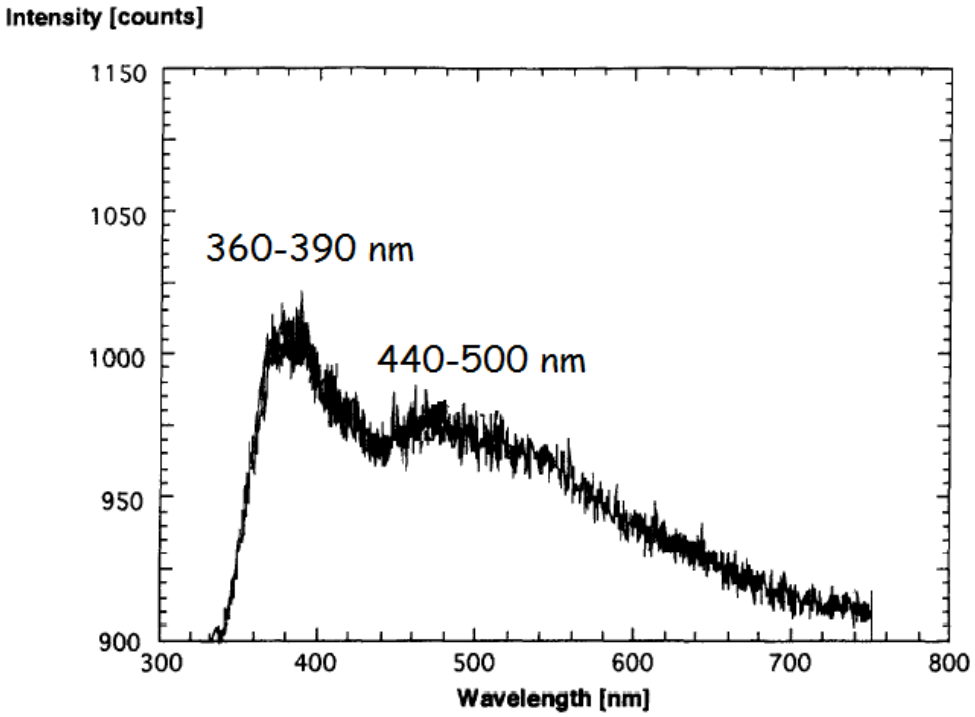

Figure 3-12: CL spectra of pure calcite [37]

Also from Table 3.1, it can be seen that the concentrations of REE are too weak to be detected by CL [36]. Moreover the same table shows also a high contet of iron (CRE S), but only at higher content of Mn (higher than 1000 ppm) and Fe (higher than 3000 ppm) the effects of CL quenching are important [37]. In fact the ion Fe^{2+} is characterized by extremely strong absorption and is the strongest quencher of visible luminescence in

minerals, having an emission band in the IR region of the spectrum. Anyway, a high amount of iron, without using LASER-ICP analysis, can be normally obtained by the EDX technique, which is available on the same apparatus where CL is performed and whose sensitivity is of about 2000 *ppm*.

Figure 3-13 shows the relation of intensity in CL, relative to Mn^{2+} and Fe^{2+} concentrations in calcite and dolomite.

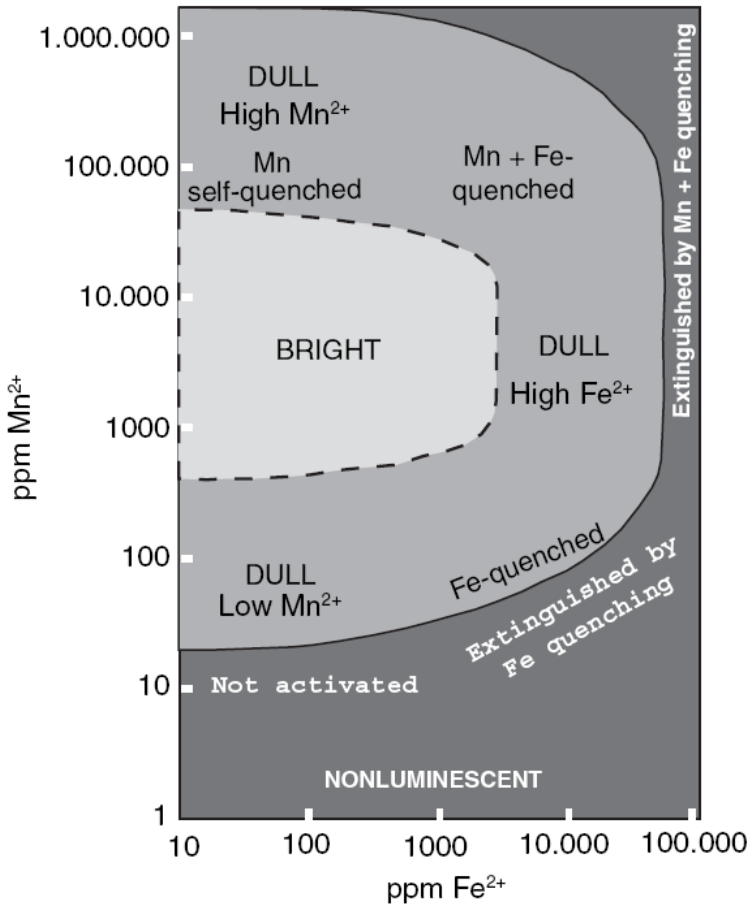

Figure 3-13: Relation of intensity in CL relative to Mn^{2+} and Fe^{2+} concentrations in calcite and dolomite. Nonluminescence is caused by low Mn^{2+} concentrations (lower left) and extinction of CL is due to Fe^{2+} quenching as well as selfquenching of Mn^{2+} (right and upper right). Cathodoluminescence is bright at moderately high concentrations of Mn^{2+} if the Fe^{2+} concentration is roughly under 2000 *ppm*. Dull luminescence at very high concentrations of Mn^{2+} is due to Mn self-quenching (upper left) and $Mn + Fe$ quenching (upper center) [38]

In our measurements we are in the region where the Mn signal is not quenched and so it increases linearly with the Mn content. So that our intention is to use our data to correlate the Mn content with the CL signal trying to obtain a calibration of our instrument by means of the more precise data supplied by Laser-ICP on the same samples.

Figure 3-14 shows ROM V CL spectra. Three peaks have been clearly individuated: the first two are related to the intrinsic defects (at 363 nm and 470 nm) and the second is linked to Mn^{2+} (620 nm).

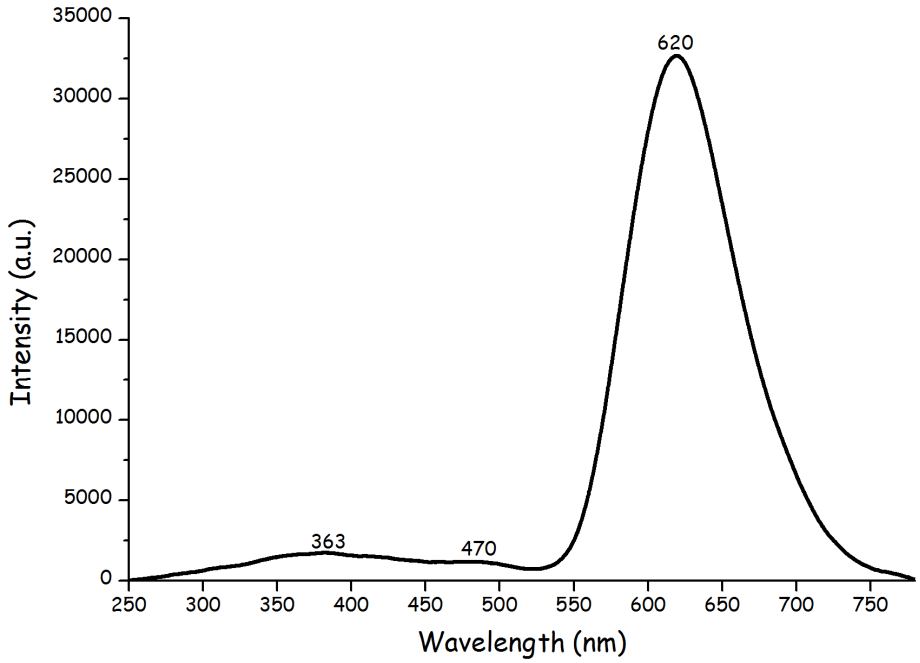

Figure 3-14: ROM V CL Spectra. Intrinsic defects (at 363 nm and 470 nm) and Mn^{2+} (620 nm) peaks are clearly visible

In order to obtain the calibration, we divided the spectrum in two areas as shown in Figure 3-15.

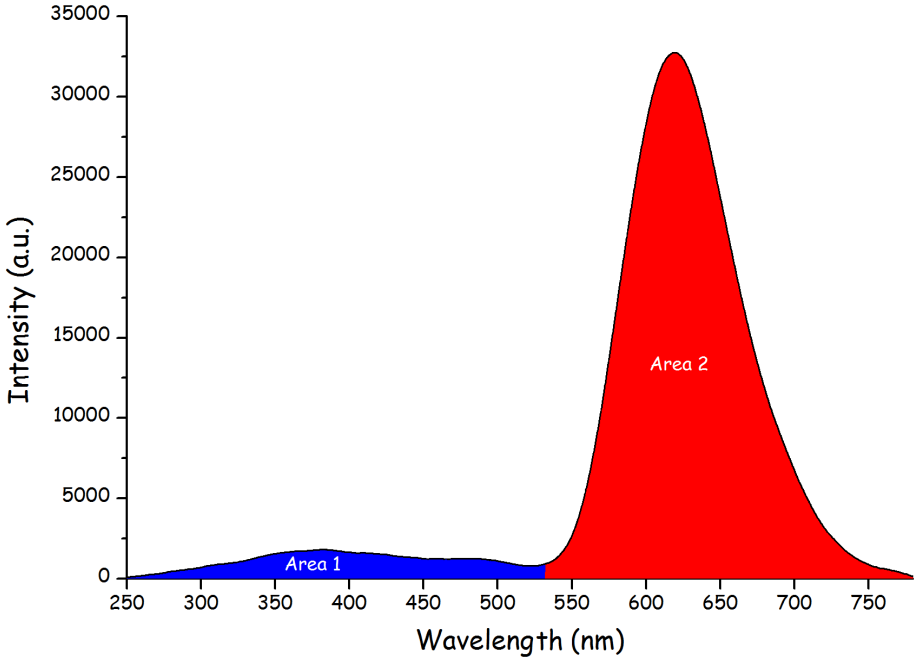

Figure 3-15: Areas considered for the calibration

Then we correlate such areas with the Mn content. Figure 3-16 shows Mn concentration versus Area 2 of all marble samples. This figure allow to say that roughly the Mn^{2+} content increases as Area 2 increases.

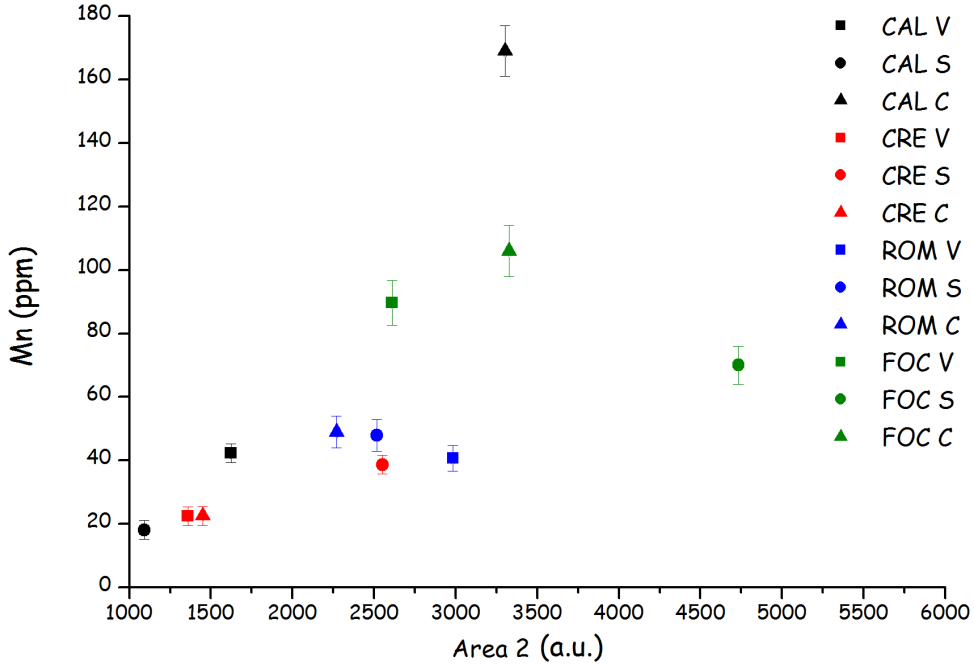

Figure 3-16: Mn concentration versus Area 2 of all marble samples

In Figure 3-17the Mn concentration is now reported versus Area 1, again considering all samples.

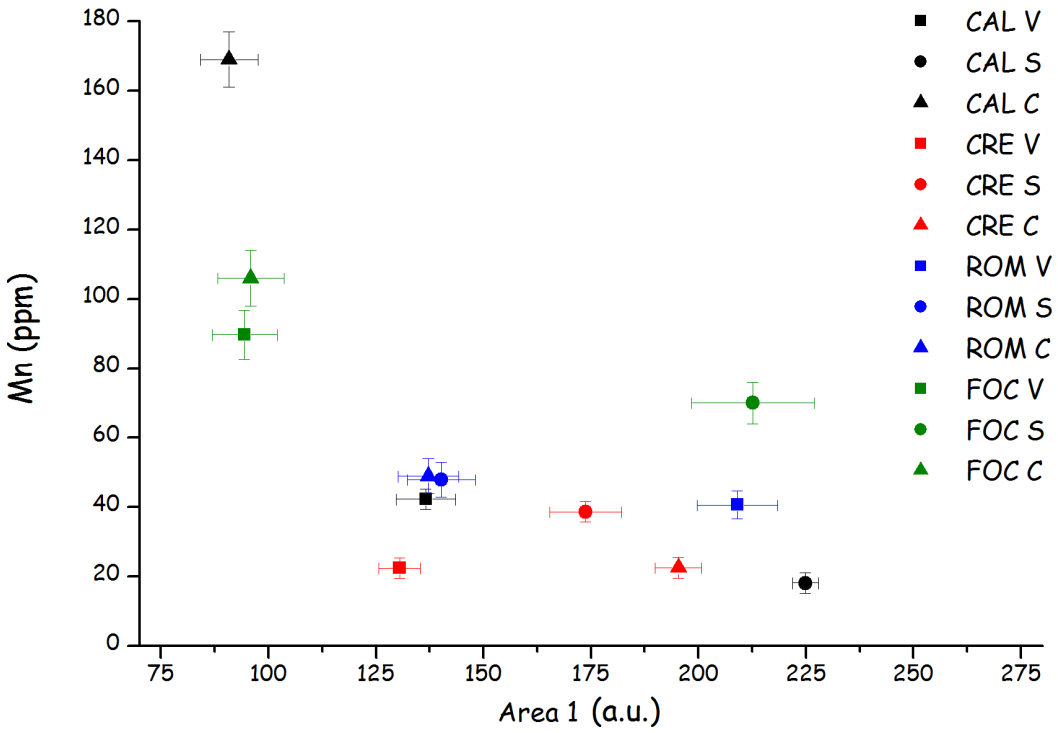

Figure 3-17: Mn concentration versus Area 1

Also in this figure we can observe a rough decrease in Mn^{2+} content as Area 1 increases (Figure 3-17). This may be attributed to the Mn strong absorption. In fact, as shown in Figure 3-18, in natural calcite emission spectra (Peak 1 at 363 nm) at room temperature (dotted curve) and Mn excitation spectrum (solid curve) overlap.

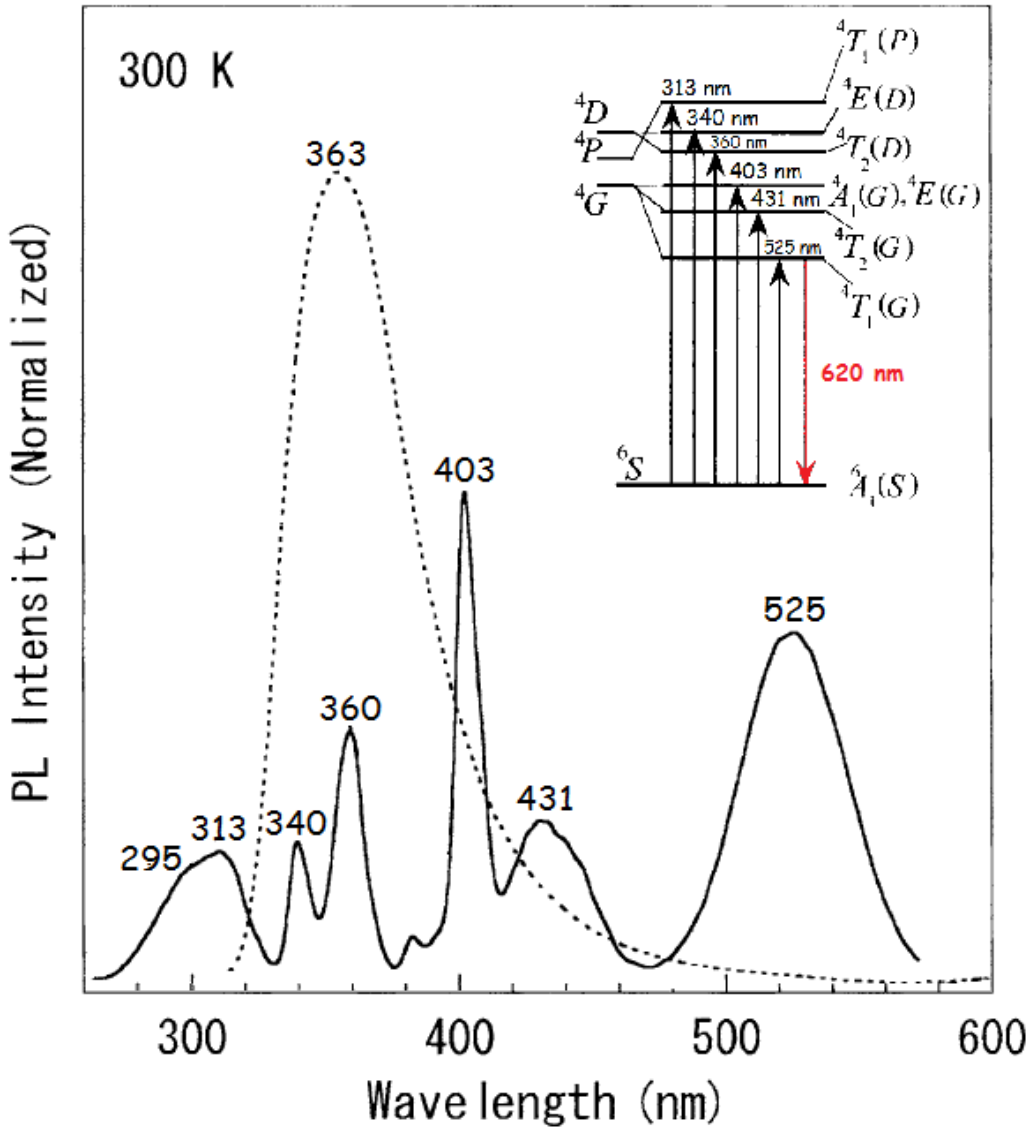

Figure 3-18: Natural calcite emission spectra (Peak 1 at 363 nm) at room temperature (dotted curve) and Mn excitation spectrum (solid curve) [21]. In the inset (top right) upward arrows and red downward arrow correspond respectively to excitation bands and emission band of Mn^{2+}.

Then, for Mn strong absorption, the intensity of Area 2 depends also on Area 1 and not only on the Mn concentration, so we can write the following proportionality:

$$Area\ 2 \propto [Mn] \cdot Area\ 1$$

This fact is confirmed by Figure 3-19 that shows a good linear correlation between Mn concentration and the ratio *Area* 2/*Area* 1 except for one single point (CAL C).

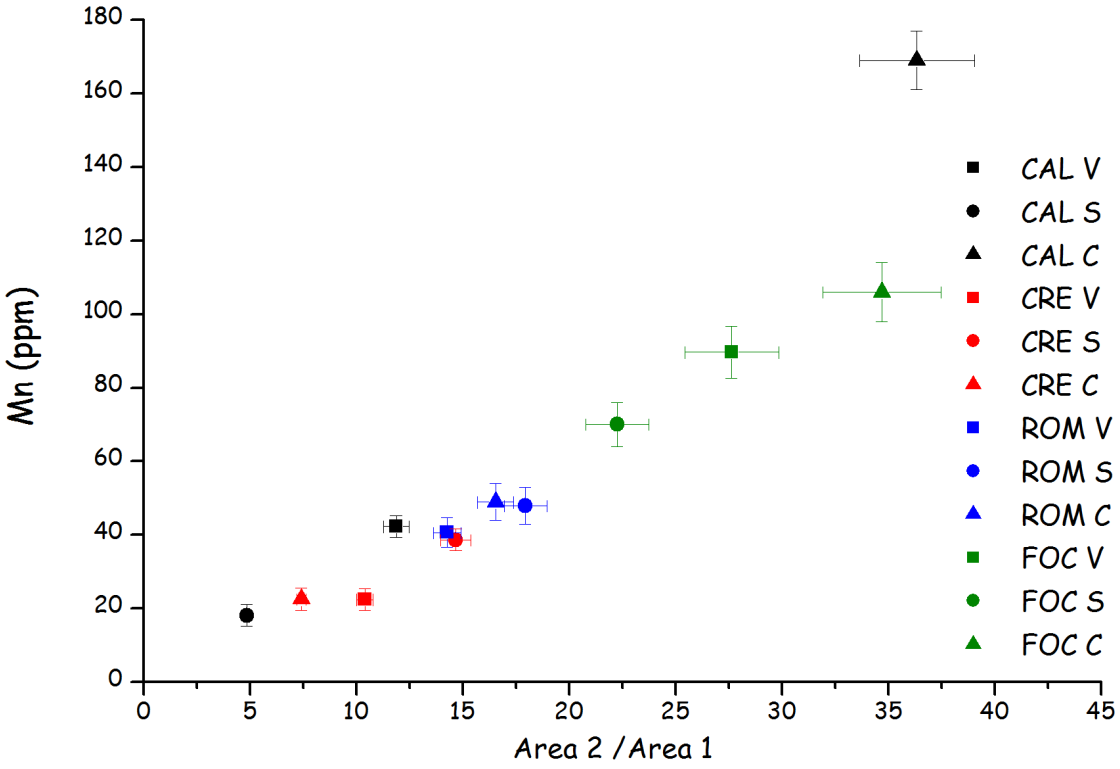

Figure 3-19: Mn concentration versus Area 2/Area 1 for all samples

But we can observe that CAL C is the sole sample with a high Mg content (Table 3.1). In fact Mg/Ca is 36% while for other samples this ratio is less than 2%. Since for all samples the CL spectra show the same main peak at 620 nm which is due to Mn^{2+} in $CaCO_3$ (while the decay of Mn^{2+} in $MgCO_3$ has his peak at 650 nm), it is better to correlate the factorized concentrations of Mn, Mg, Ca, expressed as $[Mn]\,(1-[Mg]\,/\,[Ca])$, with the ratio *Area* 2/*Area* 1. As shown in Figure 3-20 the correlation is very satisfactory, obviously, it was assumed an equal distribution of Mn^{2+} in both sites, $CaCO_3$ or $MgCO_3$.

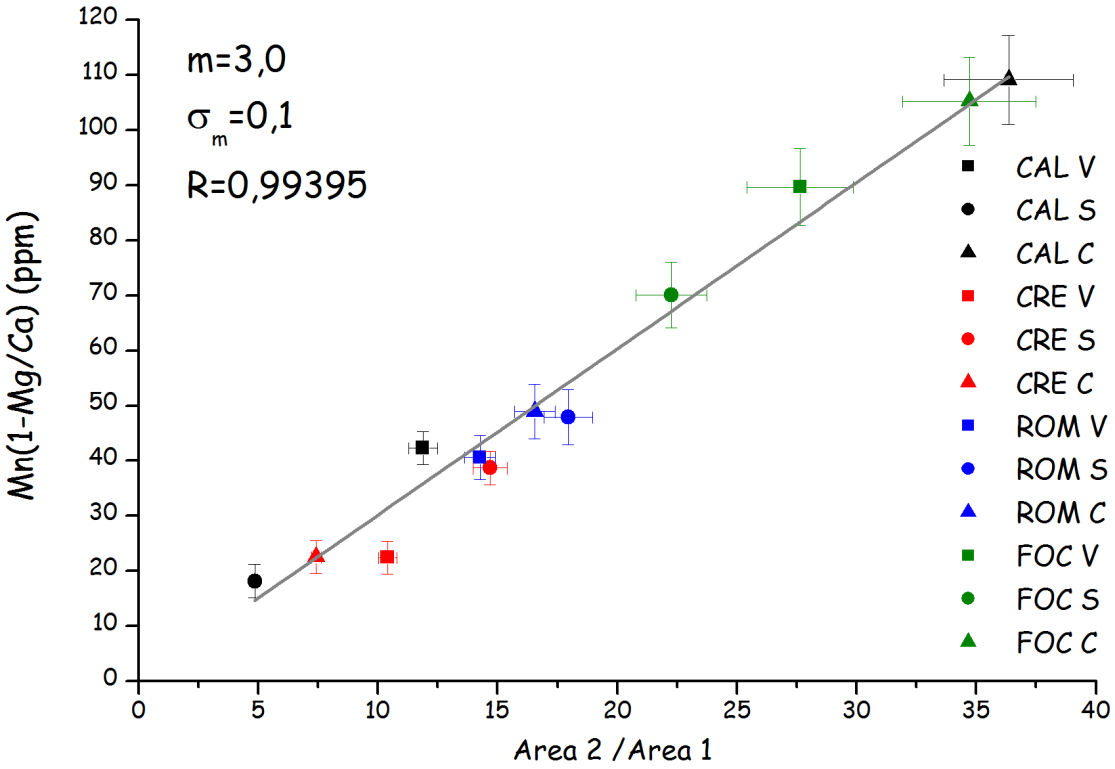

Figure 3-20: [Mn](1-[Mg]/[Ca]) concentration versus Area 2/Area 1 of all marble samples. In the inset (top left) slope and correlation coefficient

In fact the parameters of the linear correlation between $[Mn]\,(1-[Mg]\,/\,[Ca])$ concentrations and the ratio $Area\ 2/Area\ 1$, are the following:

Slope:

$$m = 3.0 \quad \sigma_m = 0.1$$

and correlation coefficient:

$$R = 0.99395$$

so we obtain a very good correlation.

3.4 Apatite

Ninety five percent of the phosphorus on Earth belongs to the minerals of the apatite group. Apatites are inorganic constituents of bones and teeth of vertebrate and man, as well as the basis of many pathologic solid formations. Minerals of the apatite group are the main raw materials in the production of phosphorus fertilizers, fodder and technical phosphates, elementary phosphorus, and phosphor-organic compounds. The mineral is sometimes substantially enriched in rare-earth elements (REE) making their extraction possible.

The apatite general formula is $Ca_5(F,Cl,OH)(PO_4)_3$. REE incorporation in apatite could give information about the chemical and structural alteration (diagenesis) of biogenic apatite [39].

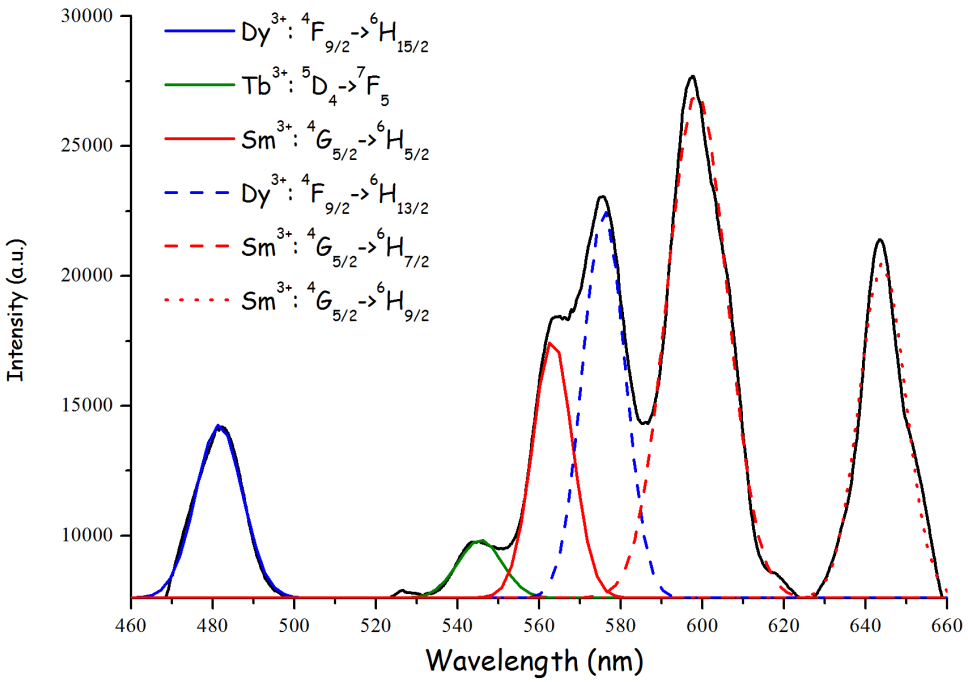

Figure 3-21: CL spectra of Apatite.

In Figure 3-21 is shown the CL detection of an apatite sample and our spectrum is quite similar to that of Gaft et al. [22] who proved that REE^{3+} are mainly built in Ca(I) position in apatite. ICP concentrations of REE, detected by CL, in our apatite sample, are 14 *ppm* for Samarium, 12 *ppm* for Dysprosium and 2 *ppm* for Terbium.

3.5 Forsterite and Enstatite

Forsterite (Mg_2SiO_4) is an olivine family member while Enstatite ($MgSiO_3$) is a pyroxenes family member; both are the major components of the earth's upper mantle [40].

The crystalline structure of Forsterite is based on a nearly hexagonal close-packed array of oxygens with Si in the tetrahedral and Mg in the octahedral sites.

The Enstatite structure consists of silica tetrahedra chains that are branched together by magnesium octahedra.

Forsterite and Enstatite crystals, owing to their good properties, e. g. refractoriness (melting point of Forsterite is 1890 $°C$), low dielectric permittivity, low thermal expansion, and chemical stability, are ideal substrates in electronics and optimal materials for thermal insulation in applications at high temperatures. The usual presence of foreign ions (Fe, Ni, Mn, etc.) in natural forsterite and enstatite and their inconstant amounts, may inhibit the high-performance of such materials [41].

In these contest we report cathodoluminescence spectra of enstatite and forsterite doped with Ti and enstatite doped with Ti and Ni during the crystallization process. The interest in doping such crystals is linked to the technology of laser efficiency [42] which can be improved by increasing the doping levels. The CL investigations provide details on the emission spectrum of the doped crystals.

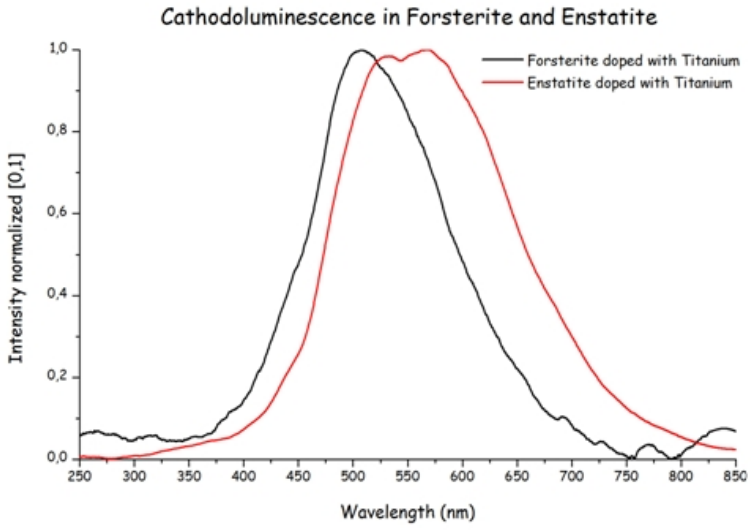

Figure 3-22: CL spectra of Enstatite and Forsterite Ti doped

In Figure 3-22 is shown the CL detection of Ti doped enstatite and forsterite. At room temperature, the CL spectrum of forsterite doped with titanium contains one broad emission located at 510 nm, while the enstatite spectrum doped with titanium contains two broad emissions located at 530 and 570 nm. The line shape of these two spectra could be related to different Ti^{4+} positions in the lattice off the host crystal [43].

In Figure 3-23 is shown the CL detection of Ni doped enstatite.

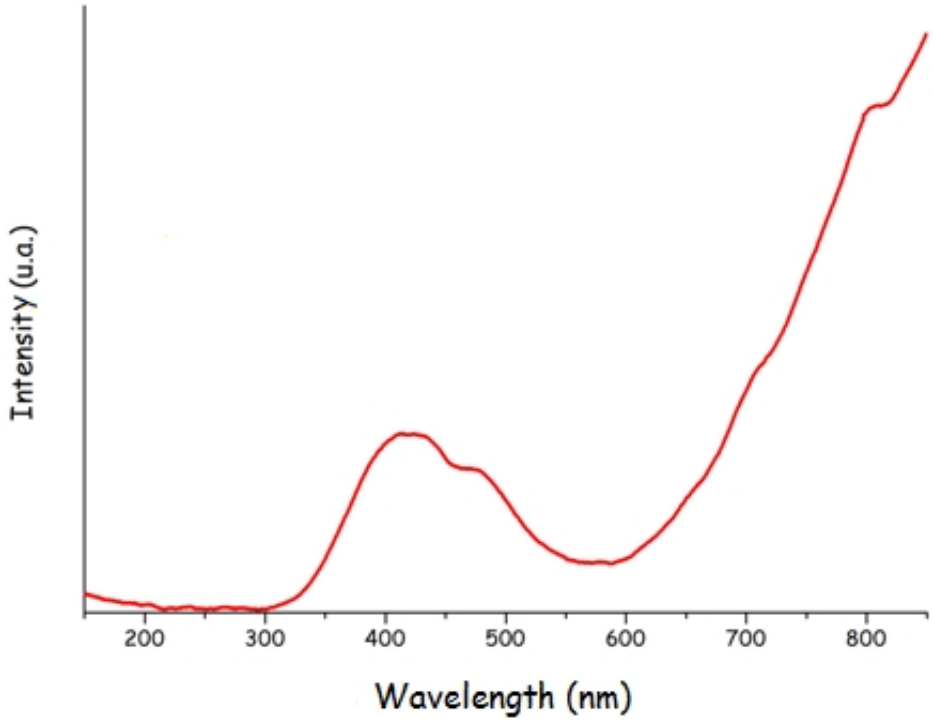

Figure 3-23: CL spectra of Ni doped enstatite

Concerning enstatite doped with nickel, the CL spectrum at room temperature contains a small broad emissions located at 410 nm with a shoulder near to 470 nm and a large broad emissions after 850 nm (Figure 3-23). This broad emission is part of the emission in the visible range of the spectrum as obtained, e.g., by Moncorgè et al. [44] in the NIR region, reported in Figure 3-24.

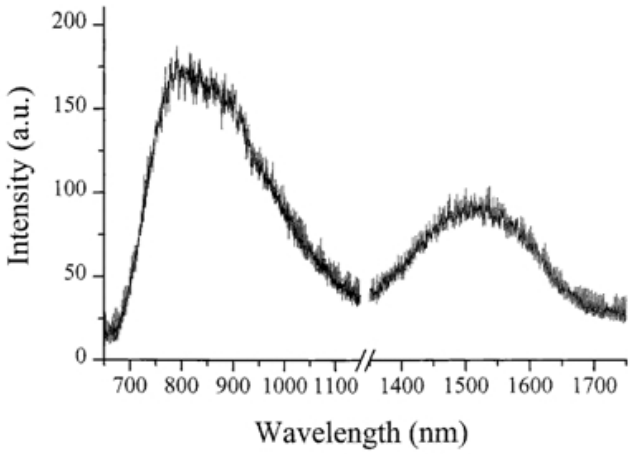

Figure 3-24: Photoluminescence spectra of Ni doped enstatite obtained by Moncorg et al. [44]

According to Ni^{2+} Tanabe-Sugano diagram for octahedral coordination, we think that 410 nm emissions is related to ${}^3T_{1g}(P) \rightarrow {}^3 A_{2g}(F)$ Ni^{2+} transition (Figure 3-23), 865 nm emissions is related to ${}^3T_{1g}(F) \rightarrow {}^3 A_{2g}(F)$ Ni^{2+} transition (Figure 3-23 and Figure 3-24) and 1520 nm emissions is related to ${}^3T_{2g}(F) \rightarrow {}^3 A_{2g}(F)$ (Figure 3-24) for a crystal filed parameter Δ near to 6600 cm^{-1}.

Ni^{2+} transitions in octahedral coordination are summarized in scheme reported in Figure 3-25.

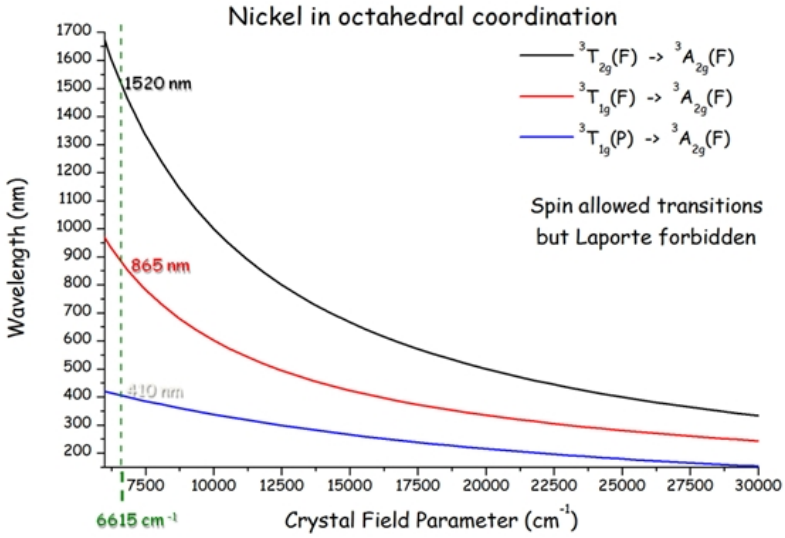

Figure 3-25: Ni^{2+} transitions in octahedral coordination

3.6 Magnetite in micro-meteorites

The study of morphology of the micrometallic spherules can supply information about the origin o such materials, in particular the detection of magnetite in such samples can support the idea of a probable extraterrestrial origin resulting from fusion of metallic meteorites as they enter the atmosphere. The examined samples are metallic micro-particles collected from rainwater of a home roof, by means of magnets. The samples vary both in size and shape: other spherical shapes, droplet-like particles were also observed. The diameter of investigated spheroidal micro-particles is between 60 and 500 μm, as showed in Figure 3-26, which is an optical image obtained from our samples.

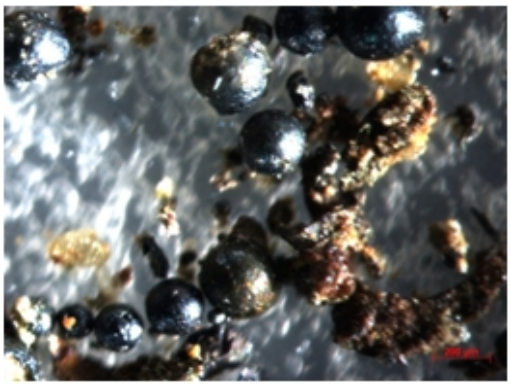

Figure 3-26: Optical image of spheroidal samples

In many case the surface morphology display polygonal structure as showed in Figure 3-27 by SEM investigation on the same samples.

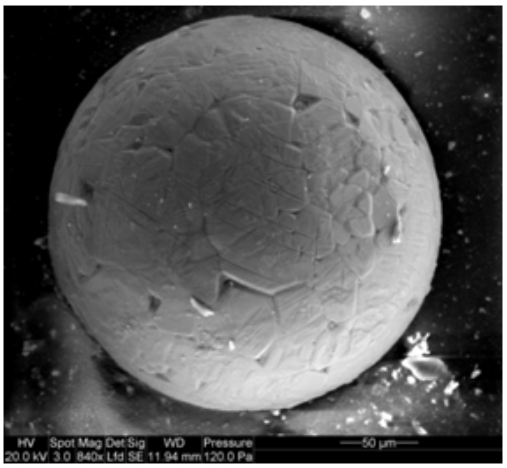

Figure 3-27: SEM image of a sample

The obtained sample composition, inspected by EDX analysis, reveals mainly the presence of iron Figure 3-28.

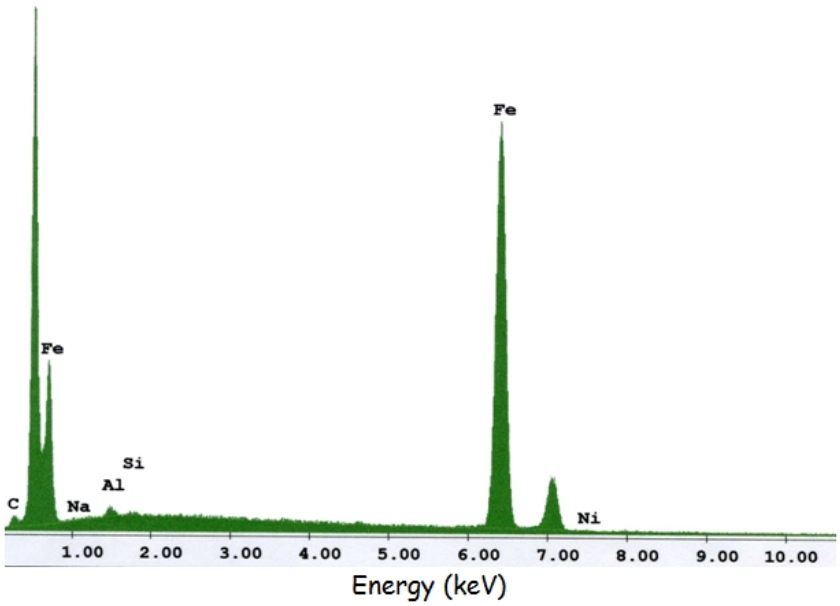

Figure 3-28: SEM-EDX analysis of a sample

But it was only by CL analysis that magnetite can be detected. In fact, as showed in Figure 3-29, at room temperature, the CL spectrum in a sample of metallic micro-particles contains two broad emissions located at $2,6\ eV$ and $3,2\ eV$.

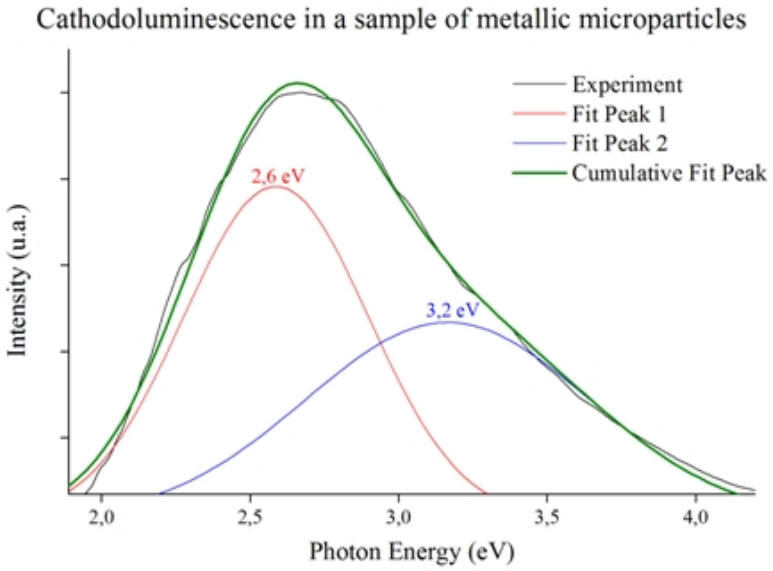

Figure 3-29: CL spectrum obtained on a micro-particle sample

The line shape of this spectrum is related to the presence of magnetite (Fe_3O_4): the strong $2,6\ eV$ peak is due to transition from the maximum in the $4s(Fe) + e_{g\gamma}$ density of states band to the maximum of the $e_{g\epsilon}$ band, and similarly the $3,2\ eV$ peak corresponds to $4s(Fe) + e_{g\gamma} \rightarrow a_{1g}$ transition, according to Balberg et al. [45] (Figure 3-30).

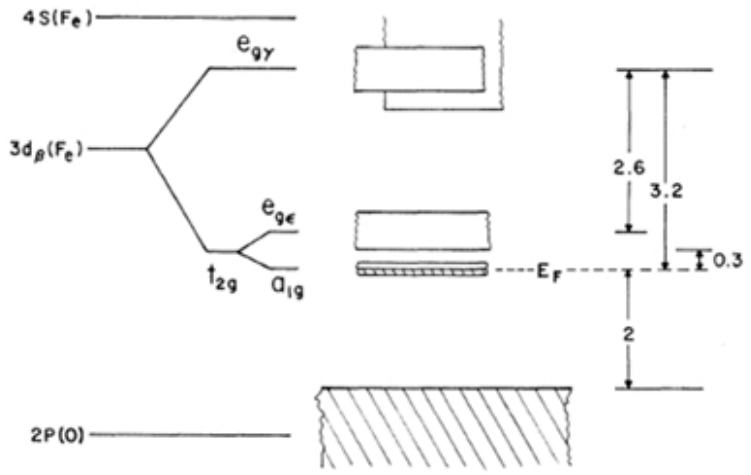

Figure 3-30: Atomic scheme level of magnetite proposed by Balberg et al. [45]

3.7 Carbon Nanotubes

Diagnostic analysis performed on Carbon Nantube samples are presented in order to find the role played by nickel oxide impurities, which is the residual catalyst material used in the growth processes [46].

The as-received pristine samples were sandwiched between two stainless steel disks without any treatment. In a second step, the samples were resistively heated.

In Figure 3-31 are shown scanning and transmission electron microscopy images of our SWCNT and MWCNT samples.

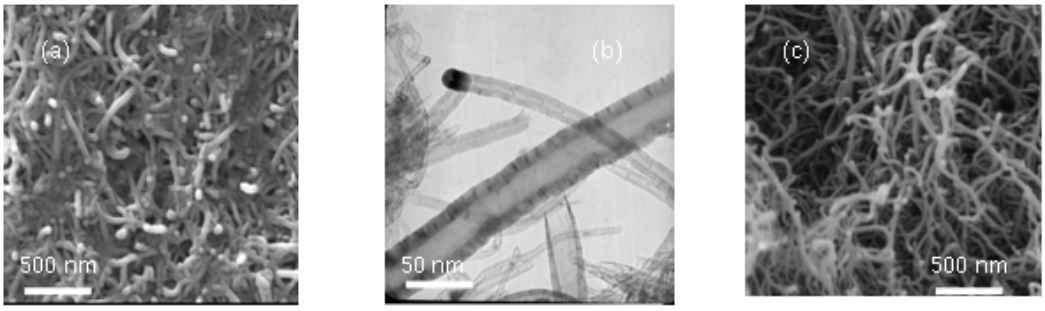

Figure 3-31: SEM and TEM images of SWCNT and MWCNT samples

It can be clearly seen (Fig. Figure 3-31a and b) that the pristine nanotubes are capped and contain large amorphous carbonaceous and catalyst particles. After annealing in vacuum (Figure 3-31c) at 1000 $^{\circ}C$ for 1 hour the nanotubes are uncapped and the amount of impurities was greatly reduced. The TEM image (Figure 3-31b) also indicates that our sample was composed of nanotubes with different number of shells and diameters.

In Figure 3-32 it is presented a set of representative CL spectra of pristine SWCNTs and MWCNTs, obtained by randomly selecting several sampling sites. Interestingly, albeit varying intensities and line shapes, all spectra show four well distinct peaks at 1.76, 1.94, 2.06, and 2.22 eV. The quite different electronic structures of multi walled and single walled carbon nanotubes then would induce us to suspect the origin of these transition lines to be extrinsic to the nanotube themselves.

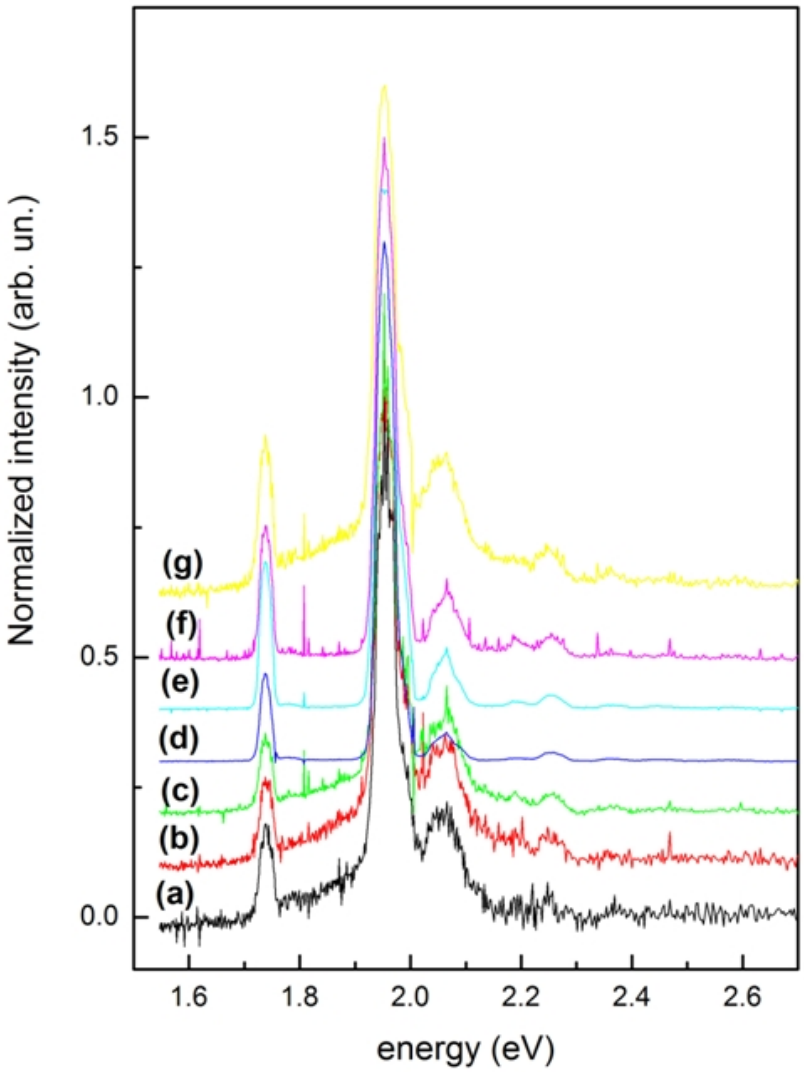

Figure 3-32: Cathodo-luminescence spectra of SWCNT (curves a, b, and c) and MWCNT backy paper samples (curves d, e, and f). These spectra were taken at randomly selected sampling sites. The top curve (g) is that for a Ni sample covered with a native oxide

To this end, we performed X-ray photoemission spectroscopy (XPS) and energy dispersed X-ray analysis (EDX) on our pristine samples. The spectra illustrated in Figure 3-33a) and b) clearly indicate the presence of Ni and O impurities and their average relative concentrations were determined with XPS to be 0.6 and 10 %, respectively.

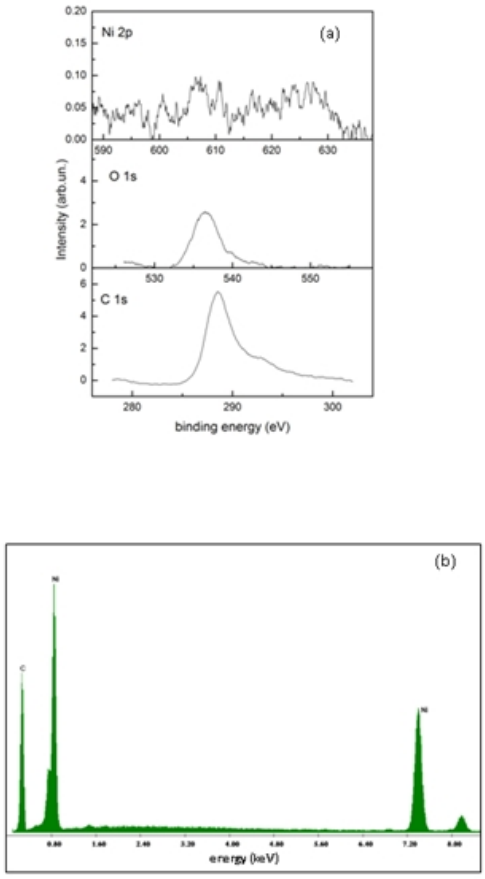

Figure 3-33: Energy dispersed X-ray analysis (a) and X-ray photoemission (b) spectra of the SWCNT and MWCNT samples

To further clarify the nature of the features seen in Figure 3-32, we have recorded the CL emission from a Ni sample covered with a thin native oxide film and the spectrum is plotted in the upper part (Figure 3-32, curve g). It can be immediately concluded that the CL signals in NTs indeed originate from the nickel oxide impurities [47][48]. These Ni particles were used as catalyst material in the nanotube growth process. After annealing at T about 1000 $^{\circ}C$ for 1 hour the luminescence emission is quenched. This is compatible with the emptying of luminescence centres caused by heating. In fact, in the usual experiments of thermo-luminescence, the system is heated until a temperature level (about $500 - 600$ $^{\circ}C$) at which all the charges are thermally excited out of their metastable levels and the luminescence completely disappears [49].

3.8 Coin Analysis

Diagnostic analysis performed on an ancient coin are presented in order to find if the coin is authentic or is a coinage proof [50].

As shown in Figure 3-34, the coin is a Drachma representing on the obverse the portrait of Poseidon and, on the reverse the figure of Anfitrite riding a seahorse while Eros is shooting an arrow. The coin is well known in the numismatic studies and originals can also be found in Catanzaro, Naples or Milan museums.

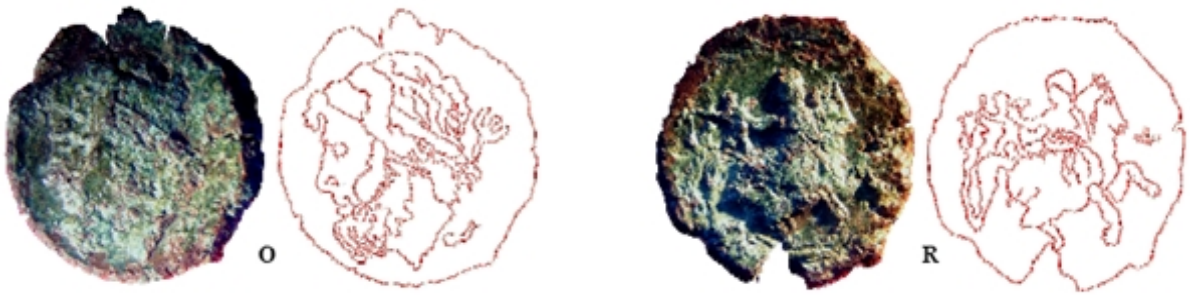

Figure 3-34: Graphic and photographic representation of the drachma. O/ Head of Poseidon with diadem on the left. On the right a trident, below a dolphin; R/ On the left Amphitrite is riding a seahorse while Eros is shooting an harrow. On the right a star.

The coin has the following characteristics:

- diameter: $15,8\ mm$
- thickness: $2\ mm$
- weight: $3,35\ g$
- Axes of the coin with orientation at 180° (Figure 3-35).

Figure 3-35: Axes of the coin with orientation at 180.

The object of the research was a coin recognized as a Bruttium product of the first decades of 3^{rd} century B.C. It was a single sample and so we had not information about the sequence of the coinage usually revealed by discovery of treasure chests. This difficulty was overcame by means of historical and macroscopic comparison with similar models kept in Catanzaro, Naples and Milan Museum.

Every observation and scientific analysis executed on this coin was put together in order to find its historical background and, at the same time, to obtain technological details about its production.

At a first glance the coins looks already in a bad state of conservation so that it was impossible to see the graphical types by naked eye: different processes of corrosion had caused a loss of material (overall on the obverse of the coin) and a chromatic alteration of metals.

The Bruttium coin was probably dated about 209 $B.C.$, that is when archeologists put the beginning of the golden coinage of Brettii.

Historical sources [51] described this people as made up by raw and savage men, shepherds, Lucani's servants which in 356 $B.C.$ created a secession's movement for the constitution of an autonomous Italian folk under the politic, economic and social profile.

Between the half of III century and the half of IV century they tried to claim the supremacy on Magna Graecia's coasts and so conquered Hipponion, Kroton and Consentia that were very important Greek towns: in this way they showed their own

power as independent state of Bruttium (that is the current Calabria).

The importance of this new political reality was strengthened by the development of a coinage in gold, silver and bronze that was identified by the ethnic expression in Greek language $\beta\rho\varepsilon\tau\tau\iota\omega\nu$.

This system of coining was independent of the roman one even if these currencies remained simultaneous during the 2nd Punic War.

Because of the federal kind of Bruttium currency it's impossible to define clearly the sites of the Bruttium mint: Arslan et al. [52] assumed that the first mint was Petelia for the bronze coinage, the second one Kroton for gold and silver and, at least, Consentia that helped Petelia.

The drachma had any reference nor graphic types but only symbols. The choice of a sea theme could refer to Kroton but the incrustation on the surface and the loss of metal made difficult reading the particulars of the coin or identifying "master symbols", useful for recognizing the authority which was responsible for that currency.

If compared to golden specimens found until now, this coin is macroscopically different for dimensions and weight. Even if it had a circular shape the coin showed visible cracks that caused a lack of integrity of the coin while thin layers of corrosion indicated the base metals. According to non-invasive and non-destructive principles the coin was studied by means of superficial technique of investigations that provided details concerning the chemical composition of the material and its alterations.

SEM image shows sample morphology, while BSE image has connected to the atomic number of elements partner in the collision process, so the obtained image in this case can be directly connected to the presence of heavier elements on the samples. At the same time on these spots was executed chemical analysis with EDX (Energy Dispersion X-ray) and luminescence emission induced by electron bombardment (CL).

The EDX analysis, executed on narrow points of the surface, revealed Pb and Cu as main components of the coin on both side: 51 % of Pb and 35 % of Cu their weight (Figure 3-36).

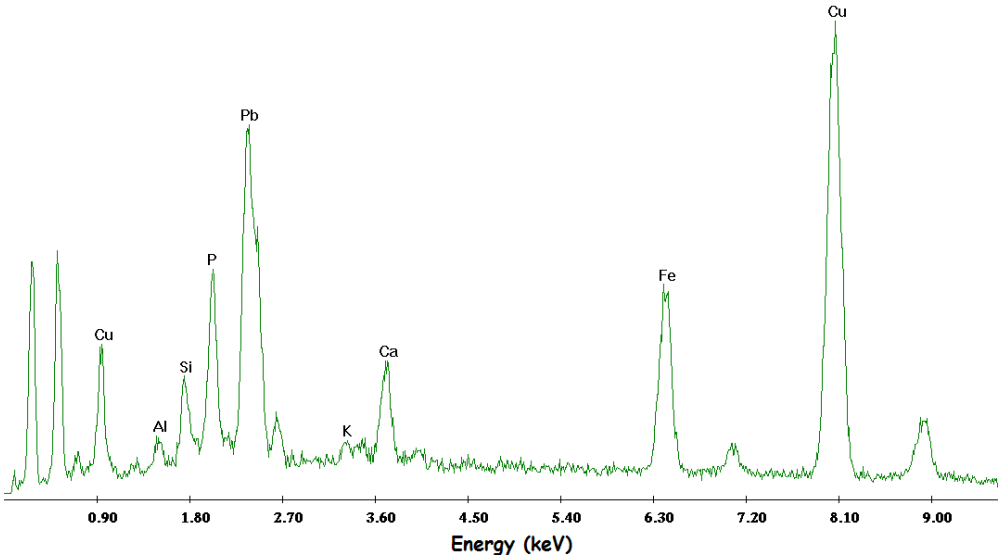

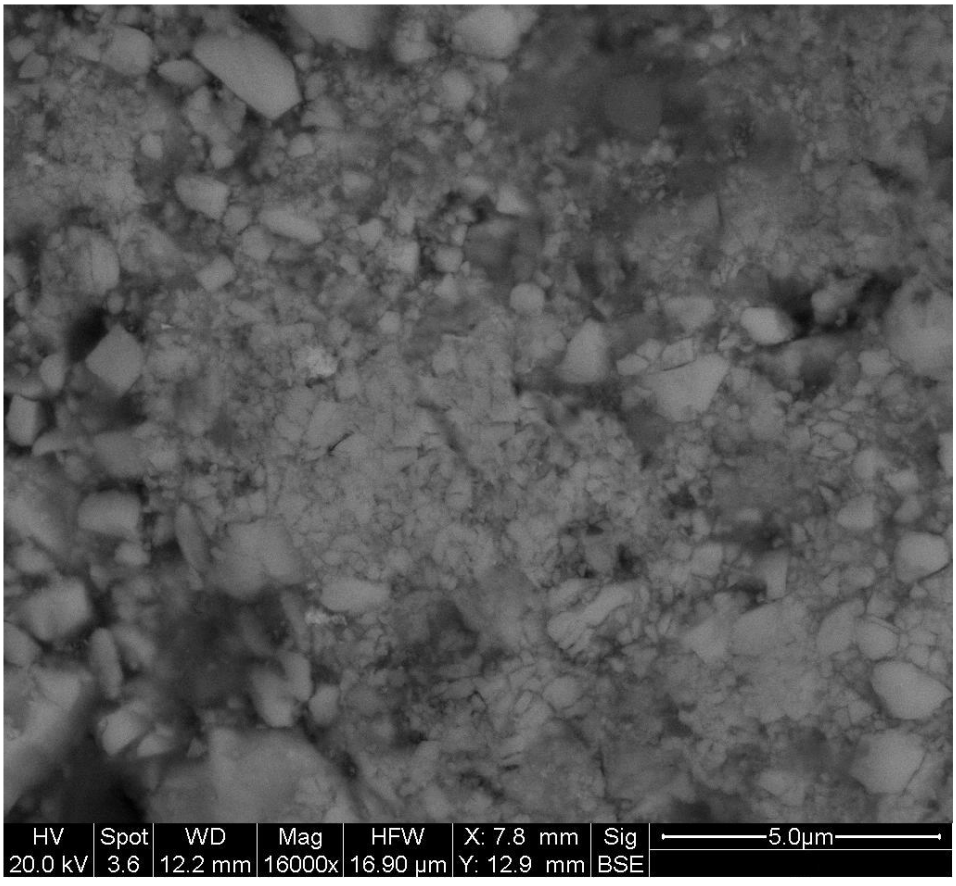

Figure 3-36: EXD spectroscopy and BSE image of Cu-Pb matrix.

Copper and lead matrix CL Spectrum is showed in Figure 3-37.

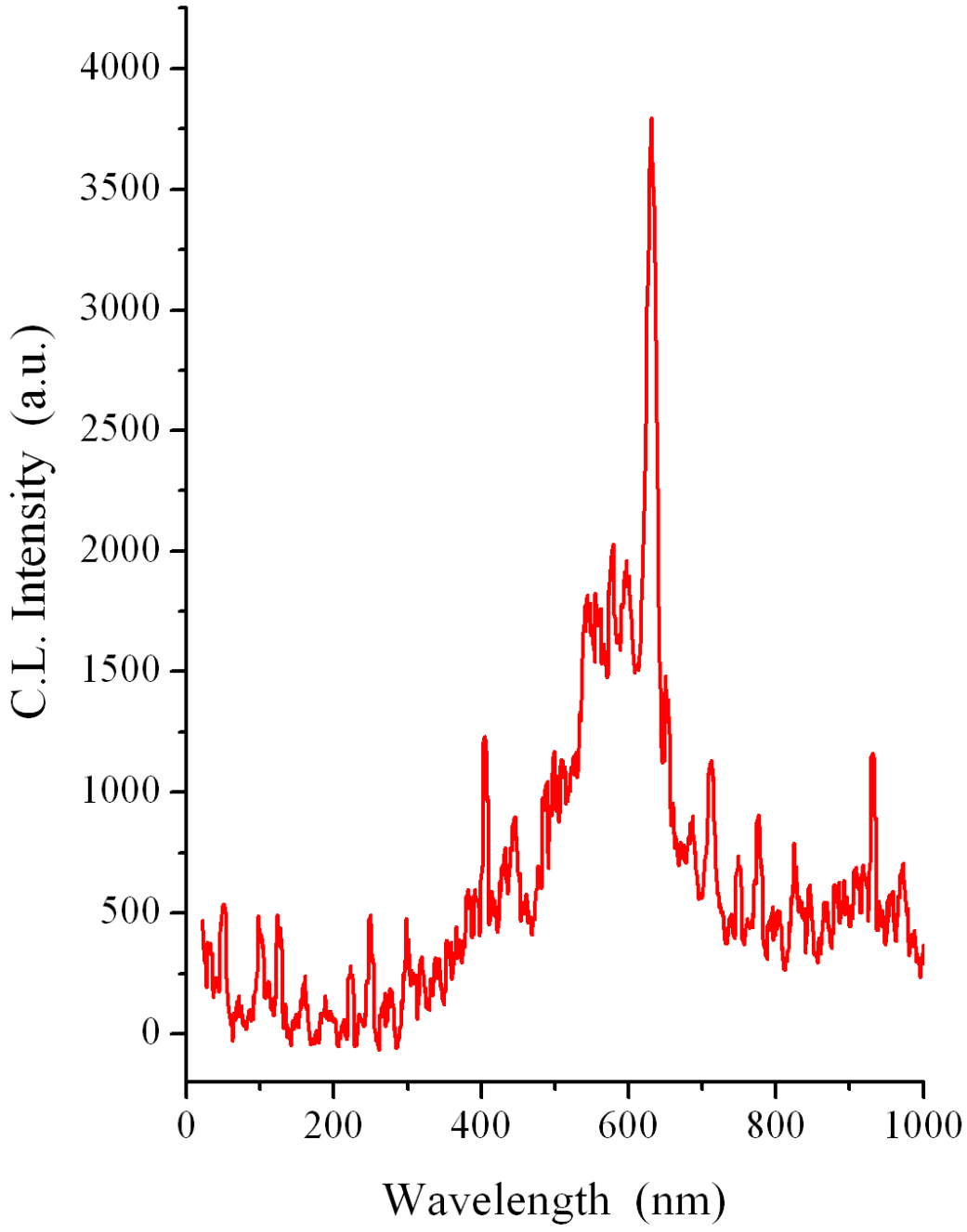

Figure 3-37: CL spectrum attributed to the copper-lead matrix

Surprisingly more intense CL spectrum (Figure 3-38), different from that associated with copper and lead matrix, was detected. As indicated in literature [53], these spectra were attributed to gold particles.

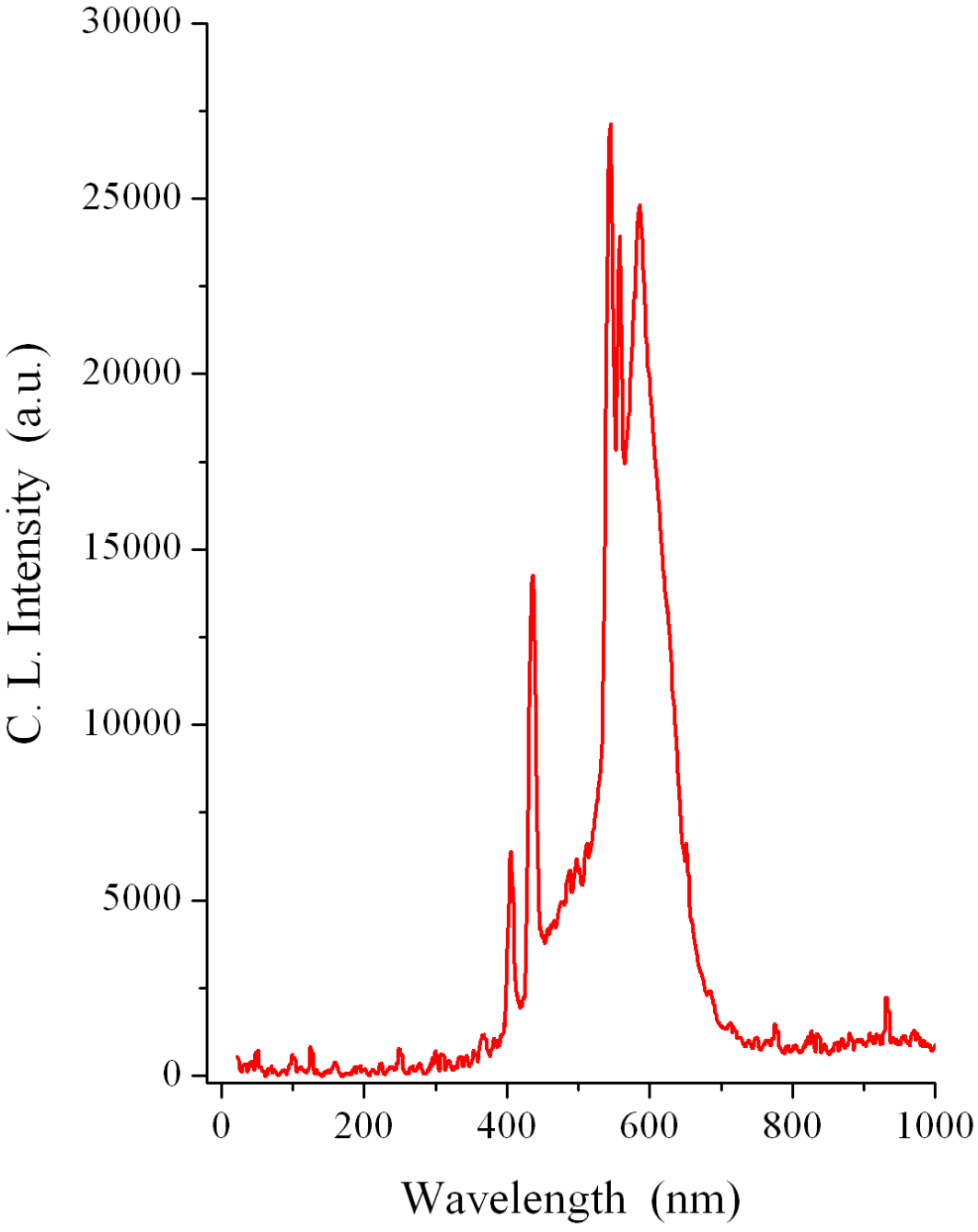

Figure 3-38: CL spectrum was attributed to gold particles

CL analysis was confirmed BSE-EDX results. In fact these latter analysis reveal that the maximum dimensions and the percentage in weight of the small spot were respectively on the order of 20 μm and 95% of gold (Figure 3-39).

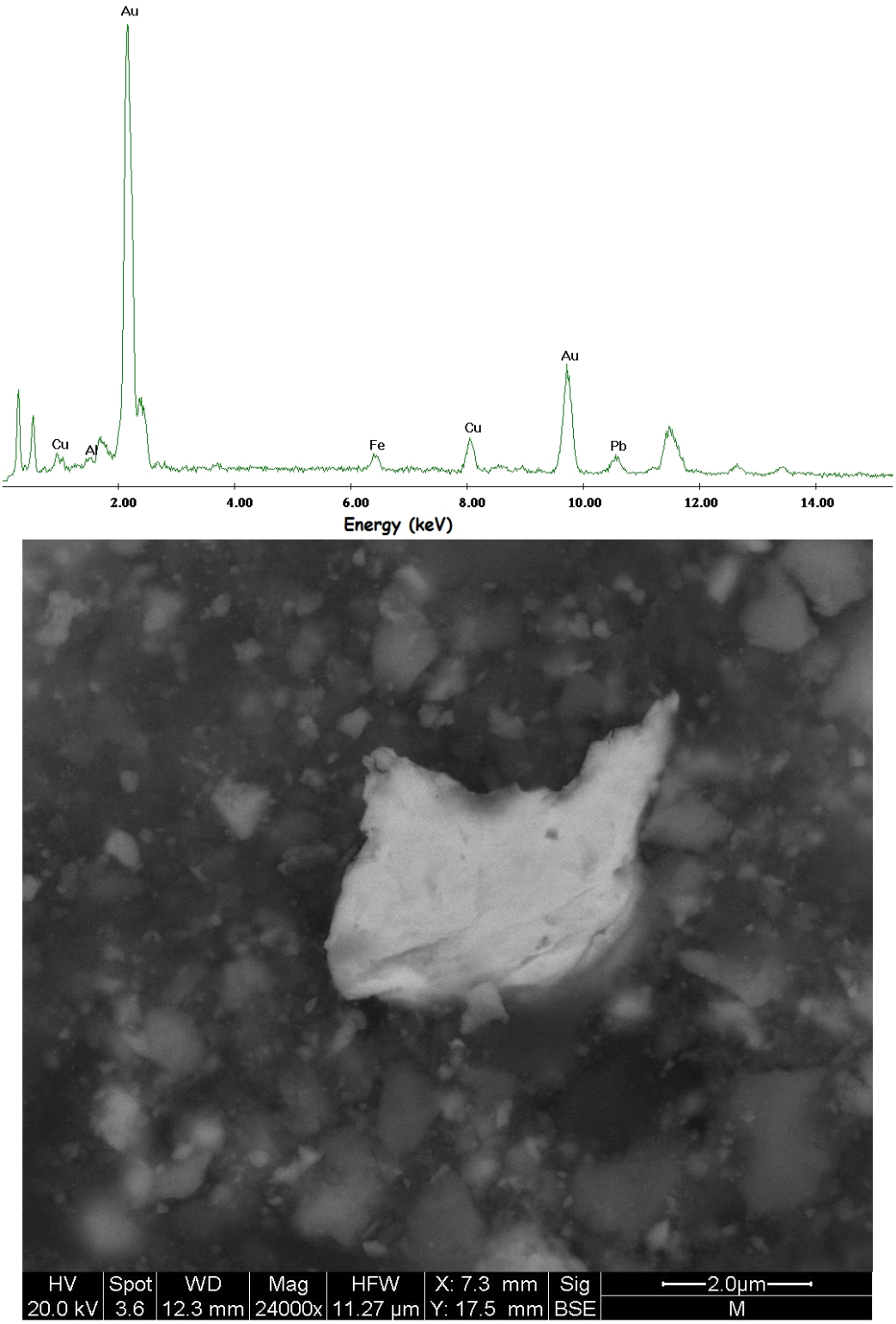

Figure 3-39: EXD spectroscopy and BSE image of Au particle

In order to detect if the presence of gold is diffused overall the coin surface, CL analysis was first carried on gold spots revealed by BSE-EDX. Then the CL beam was moved in various position on the sample and the same spectrum at 620 nm (attributable to gold) has been detected in several positions (eyebrows, beard, fork on the Head of Poseidon on the obverse of the coin, horse hoof on the verso), revealing that gold was probably covering all the surface coin on both sides.

The presence of traces of gold on surface coin on both sides is in contrast with the fact that the coins of the same age present in museums are hard gold.

Then this coin was probably only plated with gold and it can be supposed two hypothesis:

1) this coin is a counterfeit money of its age

2) the coin is a coinage proof contaminated by the residual gold in the cast.

The most likely hypothesis is the first for several reasons:

a) the coin weight and size are reduced with respect to the originals in hard gold;

b) the coin matrix is in Pb and Cu, while the proofs are normally in bronze;

c) the gold traces are on both sides (obverse and reverse);

d) the styling of the coin is rather accurate in the details;

e) some iconographic details are rather similar to other golden bruttian coinage.

Conclusions

The main goal of the thesis consisted in realizing an apparatus of CL starting from an old SEM and this scope has been reached with success. The performances of the new instrument, with our low cost modifications, are equivalent to a standard SEM-CL apparatus the cost of which, on the market, is much more expensive. Such performances have been validated using well known spectra of the literature as benchmark. Then new applications (such as Cl on carbon nanotubes or individuation of some components in micro meteorites or the identification of spectra taken on enstatite and forsterite) have been designed by performing accurate measurements and prospecting new research developments.

Moreover additional potentiality of our SEM-CL apparatus have been verified by defining a calibration of the instrument using data acquired, on the same identical samples, via Laser-Induced Coupled Plasma analysis (LA-ICP), which is a technique very sensible to traces of elements (up to $10 - 100$ *ppb*). However, as it is well known, the LA-ICP technique is a destructive technique, while the CL analysis is not. Indeed adding a CL analysis to the standard investigation possibilities of a SEM one can obtain, simultaneously and non destructively on the same spot: luminescence spectra, SEM-BSE images and also chemical analysis by EDX (Energy Dispersion X-ray). In particular, using luminescence signal obtained from calcite samples, it was possible to obtain a calibration from which Mn contents are appreciable up to a few ppm.

Finally an interesting application has also been obtained in the field of Cultural Heritage by investigating some properties of an old Bruttium coin, for which we formulate the hypothesis that the coin is probably a counterfeit money of its age.

Publications inherent the work of this thesis

Publications

Pingitore V., Barberio M., Davoli M., Gattuso C., Noce N., Oliva A. - *A golden dracma from Bruttia: a counterfeit money revealed by Scanning ElectronMicroscopy and Cathodoluminescence* - Journal of Mediterranean Archeology and Archeometry 2008, Vol. 8, n. 2, pp. 31-38

Pingitore V., Oliva A., Barberio M., Barone P., Camarca M., Bonanno A., Xu F. - *Visible Cathode- Luminescence from Carbon Nanotubes: The Role of Impurities* - Physica Status Solidi A, 2008, Vol. 205, n. 6, pp. 1391-1393

Conferences

Pingitore V., Oliva A., Barberio M., Barone P., Camarca M., Bonanno A., Xu F. - *Visible Cathode-luminescence from Carbon Nanotubes: The Role of Impurities* - Trends in NanoTechonology 2007 03-07 Settembre 2007 San Sebastian (Spain) – Poster

Pingitore V., Oliva A., Barberio M., Barone P., Camarca M., Bonanno A., Xu F. - *Preliminary results on transport properties of alkali-metal-doped Single-Wall carbon Nanotubes mats* - Chemical NanoTechonology Talks VIII 20-21 Novembre 2007 Francoforte sul Meno (Germany) – Poster

Pingitore V., Oliva A., Barberio M., Barone P., Camarca M., Bonanno A., Xu F. - *Transport properties of alkali -doped single –wall carbon nanotubes mats* - NanoSmat 2008 21-24 Ottobre 2008 Barcellona (Spain) – Talk

Contributions to Conferences

Pingitore V., Barberio M., Davoli M., Gattuso C., Noce N., Oliva A. - *La contraffazione di una moneta aurea di fattura bruzia rilevata dall'uso combinato della microscopia a scansione elettronica (SEM) e della catodoluminescenca (CL)* - V Congresso Nazionale di Archeometria "Scienza e Beni Culturali" (26-29 Febbraio - Siracusa)

Pingitore V., Bloise A., Barrese E., Apollaro C., Miriello D. - *Flux growth and characterization of Ti- and Ni- doped enstatite single crystals* - Convegno "FIST", Rimini 2009

Pingitore V., Miriello D., Chiaravalloti F., Bloise A., Barca D., Crisci G. M., Oliva A. - *Characterization of magnetic microspherules: preliminary results* - Geoitalia, Rimini 2009

Bibliography

[1] Y. Tanabe, S. Sugano. J. Phys. Soc. Jpn. 9 753 (1954)

[2] Y. Tanabe, S. Sugano. J. Phys. Soc. Jpn. 9 766 (1954)

[3] H.H. Tippins. *Charge-Transfer Spectra of Transition-Metal Ions is Corundum.* Phys. Rev. B 1 126 (1970)

[4] S.W.S. McKeever, B. Jassemnejad, J.F. Landreth. *Manganese Absorption in CaF2 : Mn.* J. Appl. Phys. 60 1124 (1986)

[5] A. Bakhtin, B. Gorobets Kazan University Publishing (in Russian) (1992)

[6] A.S. Marfunin *Methods and instrumentations: Results and recent developments.* Springer, Berlin Heidelberg New York. Advanced Mineralogy. Vol.2 (1995)

[7] B. Henderson, G.F. Imbusch. *Optical Spectroscopy of Inorganic Solids.* OxfordUniversity Press, UK (1989)

[8] M. Born, J.R. Oppenheimer. Ann. d. Physik 84 457 (1927).

[9] H. Yamamoto. *Phosphor handbook: Fundamentals of luminescence.* CRC Press LLC, Boca Raton (1999).

[10] M.D. Sturge. Solid State Phys. 20 91 (1967).

[11] B.R. Judd. *Optical Absorption Intensities of Rare-Earth Ions.* Phys. Rev. 127 750 (1962).

[12] G.S. Ofelt. *Intensities of crystal spectra of rare-earth ions.* J. Chem. Phys. 37 511 (1962).

[13] H. Forest, G. Ban. J. Electrochem. Soc. 116 474 (1969).

[14] G.H. Dieke, edited by H.M. Crosswhite, Hannah Crosswhite. *Spectra and Energy Levels of Rare Earth Ions in Crystals.* John Wiley & Sons, USA (1968)

[15] D. Langer, S. Ibuki. *Zero-Phonon Lines and Phonon Coupling in ZnS:Mn.* Phys. Rev. 138 A809 (1965)

[16] G. Walker, Chem. Britain, 19,824-31 (1983). *Mineralogical applications of luminescence techniques.* In Chemical Bonding and Spectroscopy in Mineral Chemistry (Berry, F. J. and Vaughan, D. J., eds.) Chapman & Hall, London, pp. 103-40. (1985)

[17] G. Walker *Luminescence spectroscopy of Mn^{2+} rock-forming carbonates centers* - Mineralogical Magazine Vol. 53, pp. 201-11 (April 1989)

[18] R.D. Shannon. *Revised Effective Ionic Radii and Ssystematic Studies of Interatomic Distances in Halides and Chalcogenides.* Acta Cryst. A 32 751 (1976)

[19] R.M. Sternheimer. *Shielding and Antishielding Effects for Various Ions and Atomic Systems.* Phys. Rev. 146 140 (1966)

[20] M. T. Hutchings. Solid State Phys. 16 227 (1964).

[21] X. Wang *Energy transfer among Pb, Ce and Mn in fluorescent calcite from Kuerle, Xinjiang, China* - Phys Chem Minerals 33:559–566 (2006)

[22] M. Gaft, R. Reisfeld, G. Panczer *Modern luminescence spectroscopy of minerals and materials.* Springer, Berlin Heidelberg New York (2005)

[23] A. Tarashchan *Luminescence of minerals.* Naukova Dumka, Kiev (in Russian) (1978)

[24] E. Kasyanenko, O. J. Matveeva Prikladn Spectroscop 46:943–949 (1987)

[25] M. Pagel, V. Barbin, P. Blanc, D. Ohnenstetter *Cathodoluminescence in Geosciences* Springer, Berlin Heidelberg New York (2000)

[26] D.J. Marshall *Cathodoluminescence of geological materials.* Allen & Unwin Inc., Winchester/Mass., 146 pp. (1998)

[27] P. Grant *The role of scanning electron microscope in cathodoluminescence petrology.* In: Whalley B. (ed): Scanning Electron Microscopy in the Study of Sediments. Geo Abstracts, pp. 1-11. (1978)

[28] N. K. Tovey and D.H. Krinsley A *cathodoluminescent study of quartz sand grains.* J. Microscopy, 120: 279-289 (1980)

[29] S.M.A. Kalceff and M.R. Phillips *Cathodoluminescence microcharacterization of the defect structure of quartz.* Phys. Review B, 52/5: 3122-3134 (1995).

[30] V.S. Lysakov *Luminescence of quartz activated with manganese ions.* Sov. Physics. J. ,21:946-947 (1978)

[31] G.T. Pott and B.D. McNicol *Spectroscopy study of the coordination and valence of Fe and Mn ions in and on the surface of aluminas and silicas.* Disc. Faraday Soc. 52: 121-131(1971).

[32] R. Chapoulie, F. Bechtel, D. Borschneck, M. Schvoerer & G. Remond *Cathodoluminescence of some synthetic calcite crystals. Investigation of the role played by cerium.* Scanning Microsc. Suppl. 9, 225-232 (1995)

[33] T. R. Wildeman, Chem. Geol. 5, 167-77 (1970)

[34] D. N. Lumsden and R. V. Lloyd, Ibid. 48, 1861-5 (1984)

[35] M. P. Lapuente, B. Turi, P. Blanc, *Marbles from Roman Hispania: stable isotope and cathodoluminescence characterization,* Applied Geochemistry 15 (2000) 1469-1493

[36] D. Habermann *Quantitative cathodoluminescence (CL) spectroscopy of minerals: possibilities and limitations* - Mineralogy and Petrology 76: 247-259 (2002)

[37] D. Habermann *Low limit of Mn^{2+} -activated cathodoluminescence of calcite: state of the art* - Sedimentary Geology 116 13-24 (1998)

[38] S. Boggs, D. Krinsley *Application of Cathodoluminescence Imaging to the Study of Sedimentary Rocks* Cambridge University Press (2006)

[39] D. Habermann, T. Gotte, J. Meijer, A. Stephan, D.K. Richter, J.R. Niklas *High resolution rare-earth elements analyses of natural apatite and its application in geosciences: Combined micro-PIXE, quantitative CL spectroscopy and electron spin resonance analyses* Nuclear Instruments and Methods in Physics Research B 161-163 846-851 (2000)

[40] G. Helffrich, Rev. Geophys. 38, 141 (2000)

[41] A. Bloise, E. Barrese, C. Apollaro, and D. Miriello, *Flux growth and characterization of Ti- and Ni-doped forsterite single crystals*, Cryst. Res. Technol. 44, No. 5, 463 - 468 (2009)

[42] I. T . McKinnie, R . Y . Choie, *Efficient laser operation of heavily doped Cr^{4+}: forsterite,* Optical and Quantum Electronics 29 605-610 (1997)

[43] Wing C. Wang, Thomas Danger, Giinter Huber, Klaus Petermann, *Spectroscopy and excited-state absorption of Ti^{4+}:$Li_4Ge_50_{12}$ and Ti^{4+}:Y_2Si0_5,* Journal of Luminescence 72-74 208-210 (1997)

[44] R. Moncorgè, M. Bettinelli, Y. Guyot, E. Cavalli, J. A. Capobianco and S. Girard, *Luminescence of Ni^{2+} and Cr^{3+} centers in $MgSiO_3$ enstatite crystals*, J. Phys.: Condens. Matter 11 6831-6841 (1999)

[45] I. Balberg and J. I. Pankove, *Cathodoluminescence of Magnetite,* Volume 27, Number 20 Physical Review Letters 15 November 1971

[46] V. Pingitore , A. Oliva, M. Barberio, P. Barone, M. Camarca, A. Bonanno, F. Xu, V*isible Cathode- Luminescence from Carbon Nanotubes: The Role of Impurities*, Physica Status Solidi A, Vol. 205, n. 6, pp. 1391-1393 (2008)

[47] I-Min Chan, Franklin C.Hong, Thin Solid Films 450 (2004) 304–311

[48] G. Wakefield, P.J. Dobson, Y.Y. Foo, A. Ioni, A. Simons, J.L. Hutchinson, Semicond. Sci. Technol. 12, 1304 (1997)

[49] C. Furetta, G. Kitis, Journal of materials science 39 2277 (2004)

[50] V. Pingitore, M. Barberio, A. Oliva, N. Noce, C. Gattuso, M. Davoli *A golden drachma from Bruttìa: counterfeit money revealed by scanning electron microscopy and cathodoluminescence* - Mediterranean Archaeology and Archaeometry, Vol. 8, No. 2, pp. 31-38 (2008)

[51] Diodoro Siculo, Bibliotheca Historica - Libro XVI, 15, 1

[52] E.A. Arslan *Monetazione aurea ed argentea dei Brettii, Ennerre*, Milano (1989)

[53] Wing-Wah Yam, Vivian; Man-Chung Wong, Keith; Hung, Ling-Ling; Zhu, Nianyong *Luminescent Gold(iii) Alkynyl Complexes: Synthesis, Structural Characterization, and Luminescence Properties*, Angewandte Chemie, 117, 3167 –3170 (2005)

Acknowledgments

I would like to express my gratitude to my supervisor, Prof. Antonino Oliva, whose expertise, understanding, and patience, added considerably to my experience.

I would like to thank the other members of my group for their assistance, Prof. Assunta Bonanno, Prof. Michele Camarca, Prof. Xu Fang, Dr. Pasquale Barone, Dr. Marianna Barberio, Dr. Davide Grosso and Dr. Roberta Vasta.

Finally, I would like to thank Dr. Mariano Davoli from the Earth Sciences Department for this technical assistance.